universität wien

MASTERARBEIT / MASTER'S THESIS

Titel der Masterarbeit / Title of the Master's Thesis

„Towards Optical Levitation in UHV: Loading using Hollow-Core Photonic Crystal Fibers“

verfasst von / submitted by

Jakob Rieser BSc

angestrebter akademischer Grad / in partial fulfilment of the requirements for the degree of

Master of Science (MSc)

Wien, 2020 / Vienna, 2020

Studienkennzahl lt. Studienblatt / degree programme code as it appears on the student record sheet:	UA 066 876
Studienrichtung lt. Studienblatt / degree programme as it appears on the student record sheet:	Masterstudium Physik
Betreut von / Supervisor:	Ass.Prof Dr.Nikolai Kiesel
Mitbetreut von / Co-Supervisor:	

Abstract

Optically levitated particles in extreme vacuum conditions are an experimental platform that may enable the generation of extended quantum states on unprecedented mass scales above 10^8 amu. Their interactions with blackbody radiation will intrinsically limit the lifetime of such states. Since the magnitude of these interactions has not yet been experimentally assessed, we propose an experiment to observe them. The aim of this thesis is to take the first step towards realizing this experiment.

We estimate the necessary experimental parameters for observing the mechanical noise introduced by blackbody interactions, i.e. free fall times of up to 10ms at pressures below 10^{-11}mBar and temperatures above 1400K. We propose an experimental design that is able to achieve these parameters. The first challenge towards this goal is reliably and deterministically loading nanoparticles into an optical tweezer at ultra-high vacuum.

The major part of this thesis focuses on the experimental implementation of a loading system to achieve this. To this end, we demonstrate the transfer of a 245nm particle from a hollow-core fiber to an optical tweezer. This method may enable loading into the ultrahigh vacuum regime in the near future.

Zusammenfassung

Im Ultrahochvakuum optisch levitierte Nanoteilchen können eine vielversprechende experimentelle Platform zur Erzeugung von ausgedehnten Quantenzuständen mit biher unerreicht großen Massen von mehr als 10^8amu in aussicht stellt. Die Lebenszeit solcher Zustände ist durch ihre Interaktion mit Schwarzkörperstrahlung limitiert. Bisher konnte dieser Effekt nicht experimentell untersucht werden. Aus diesem Grund schlagen wir hier ein Experiment vor, das erlauben soll den Einfluss der Schwarzkörperstrahlung auf die Bewegung eines Teilchens zu beobachten. Im Rahmen dieser Arbeit nehmen wir die ersten Schritte die zur Umsetzung dieses Experiments führen.

Zum einen schätzen wir die experimentellen Parameter ab, die notwendig sind um die Auswirkungen der Schwarzkörperstrahlung sichtbar zu machen. Es zeigt sich, dass hierfür eine Freifallzeit von bis zu 10 ms bei einem Vakuum von 10^{-11}mBar und einer Temperatur über 1400K nötig sind. Desweiteren diskutieren wir einen experimentellen Aufbau, der dieses Parameterregime erreichen sollte. Die erste Herausvorderung auf dem Wegs stellt das reproduzierbare Laden von Nanoteilchen in optischen Fallen im Ultrahochvakuum dar.

Den Großteil dieser Arbeit befaßt sich mit dem experimentelle Aufbau eines solchen Lademechanismums. Aufbauend auf früheren Experimenten zum Transport von Nanoteilchen in Hohlfasern zeigen wir hier die erfolgreiche und reproduzierbare Übergabe von 245nm großen Teilchen von der Hohlfaser in eine optische Pinzette. Unsere Methode ebnet den Weg für eine schnelle und einfache Quelle von Nanoteilchen für verschiedenste Experimente zur optischen Levitation im Ultrahochvakuum.

LIST OF FIGURES

CONTENTS

INTRODUCTION

The preparation of massive particles in superposition states has made great progress in recent decades. Interference experiments were performed with masses ranging from electrons up to large bio molecules in the order of 10^4 amu [1]. In the long run, superpositions of masses that even have an observable gravitational effect can become possible. In this uncharted terrain, new physics can become relevant. However advancing to masses large enough to observe such effects experimentally is a major challenge.

Optical levitation experiments have become a promising contender towards realizing quantum experiments for mass scales above 10^8 amu. The optomechanical tools available and the superior decoupling of such systems from their environment allow for precise motional detection and control. Several approaches were proposed to realize massive superposition of sufficient magnitudes (e.g. [2] [3]). By now, the progress in motional control and cooling of optically levitated particles has made it possible to reach the motional ground state [4] [5], paving the way for experiments in the quantum regime at mass scales of 10^9 amu.

The major challenge in improving the lifetime of the quantum states in such experiments is decoherence of the state due to interactions with the environment. The main sources of decoherence in optical levitation are interactions with the trapping light, the surrounding gas and blackbody radiation.

For a particle confined to an optical trap the scattered light will lead to a constant decoherence of quantum states. This fundamentally limits the lifetime of states in which a trapped particle can be prepared. In addition to this fundamental source of decoherence, phase and intensity fluctuations of the trapping beam lead to further reductions in state lifetime and heating of the particle motion. Optical levitation, in contrast to other optomechanical systems, allows free fall experiments to be performed, which are being proposed to circumvent this issue [6].

Due to their small de Broglie wavelength, scattering of background gas has a much larger effect on the coherence for a single interaction. A single scattering event can destroy a complex quantum state entirely. For this reason such events must be avoided. This can be achieved by lowering the ambient pressure, which reduces the scattering frequency with gas particles.

Decoherence due to emission, scattering and absorption of blackbody radiation has a significantly smaller effect, due to the longer wavelength and lower intensity. It can only be observed in the absence of recoil heating from the optical tweezer light, in other words, when the optical trap is off. Depending on the relevant temperatures [7], it also requires sufficiently low pressures which are typically in the XUHV regime. Among these mechanisms interaction with blackbody radiation is the only contribution without intrinsic limit and may well prove to be the ultimate factor limiting the realization quantum superposition states at macroscopic mass scales.

This thesis represents the first step towards an experiment that measures the effect of blackbody radiation on levitated nanoparticles. Once successful, this endeavor will provide the necessary experimental foundation to precisely predict the effects of blackbody decoherence and optimally design experiments for the preparation of massive, macroscopic quantum superposition states in levitated nanoparticle experiments. Another opportunity is the verification of Plack's law for a microscopic system, testing for predicted deviations from the theory at such scale [8][9]. The underlying idea is focusing on observing the diffusive effect of random force noise introduced by blackbody radiation, rather than the decoherence itself, avoiding the preparation of superposition states to start with.

By directly measuring the magnitude of momentum diffusion introduced to a nanoparticle due to interaction with blackbody radiation we can find the ultimate limit to the lifetime of quantum states in optical levitation experiments.

Here, we estimate the experimental parameters needed to observe blackbody radiation diffusion effects, demonstrating that they are all in reach of current state-of-the-art technology. We show that the major milestone that

needs to be achieved beyond state-of-the-art levitation is optical trapping at 10^{-11} mBar, in an experiment that allows nanoparticles to be loaded directly into UHV. However, experiments till now operate in pressures above 10^{-9} mBar, [10], [11]. To this end, the major part of this thesis focuses on the development of a UHV compatible particle loading scheme, with the handover of a nanoparticle from a HCPCF to an optical tweezer, building on previous work by Grass et al [12].

The thesis is structured as follows: The first chapter will discuss the necessary parameters for observing blackbody induced momentum diffusion. With these parameters we then propose an experimental setup, that is able to achieve the required conditions.

In chapter two the physics behind optical trapping in the Rayleigh regime is discussed for configurations relevant to our experiment.

Chapter three gives a short overview of the state of the art in optical levitation, experimental limitations imposed by the requirement of extreme vacuum levels, as well as an overview of loading solutions.

In chapter four we present the experimental setup with which the transfer of nanoparticles between optical conveyor belt and optical tweezer was achieved.

Chapter five describes the alignment procedure and analyses the experimental data of handovers between conveyor belt and optical tweezer, as well as the combined optical trap.

Finally, the results of the experiment are contextualized in a roadmap towards the experimental observation of blackbody radiation induced diffusion and we discuss the next steps towards experimental realization.

EXPERIMENTAL PROBING OF BLACKBODY RADIATION INDUCED DIFFUSION

Even in the absence of background gas and trapping light a test particle will emit, scatter and absorb blackbody radiation. These interactions will fundamentally limit future experiments on the macro scale, that aim to observe quantum effects like interference or entanglement. For this reason it is essential to have proper understanding of the interactions taking place. The historical treatment of blackbody radiation by Max Plank [13] is limited to objects much larger than the wavelength. The applicability of the standing theory to subwavelength scatterers is an open question. Recent theoretical work suggests that a strong divergence from Planck's theory might occur in this regime [14]. Such a violation of Planck's theory was recently observed in an experiment [15], where effects deviated by orders of magnitude from those predicted by Planck's theory.
To properly model the interactions and plan future experiments in the quantum regime, a more complete understanding is vital. For this purpose, we propose here an experiment to quantify the influence of blackbody radiation on levitated nanoparticles.

Levitated nanoparticles present themselves as a good system for measuring blackbody diffusion, since motional control and positional sensitivity allow for detecting the ground state movements of the particles. By cooling a levitated particle to the motional ground state, letting the wave-packet evolve in free fall and finally measuring the position of the particle over many trial the deviations from free quantum evolution according to Schrödinger can be tested.

Environmental Decoherence

The theory of environmental decoherence provides a powerful tool to quantify the magnitude and effects of interactions a quantum system has with its surroundings. Introduced by E.Joos and H.D.Zeh in 1985 [16], this theory models the interactions with environmental particles, like photons or gas par-

ticles and makes predictions for the effect these have on a wavefunction.

The main idea is to use the predictions coming from decoherence theory applied to the case of black body photons to estimate the magnitude of the diffusion effects. This section aims to give an overview of environmental decoherence relevant to the goal of observing blackbody diffusion.
E. Joos and A.D. Zeh specifically considered contributions in two limiting cases, the short wavelength limit and the long wavelength limit. Both forms of decoherence contribute to an accelerated expansion of the wave packed width beyond what is predicted for a free particle.

The short wavelength limit describes scattering with particles, whose ground-state extension is much larger than the (equivalent) wavelength of the scattering particle. Particles in this regime are usually molecules or small particles that, due to their short deBroglie wavelenght, can resolve the position in a single scattering event. Since the rate of scattering with constituent particles of a background gas is dependent on the pressure, one can suppress this contribution by using increasingly higher levels of vacuum.

The long wavelength limit covers interactions in the limit where the ground-state extension is much smaller than the wavelength of scattering particles. The contributors to this form of decoherence are mostly thermal photons. Such interactions do not resolve the position of the particle perfectly after a single scattering event, but as the number of scattered photons is very large the coherence time can be severely affected.

The diffusion due to blackbody radiation fall into the long wavelength limit. According to [17] they are given by:

$$\Lambda_{bb,e/a}(T_{i,e}, r) = \frac{16\pi^5 a^3 c}{189}\left(\frac{k_B T_{i,e}}{c\hbar}\right)^6 Im\left[\frac{\epsilon-1}{\epsilon+2}\right], \tag{1}$$

$$\Lambda_{bb,sc}(T_e, r) = 8!\frac{8a^6 c}{9\pi}\left(\frac{k_B T_e}{c\hbar}\right)^9 Re\left[\frac{\epsilon-1}{\epsilon+2}\right]^2, \tag{2}$$

where a is the radius of the test particle $T_{i,e}$ the internal and external

temperatures, ϵ the dielectric constant of the material, $\hbar$ the reduced Planck constant, c the speed of light and k_B the Boltzmann constant. These are the absorption, emission and scattering contributions to the blackbody radiation induced diffusion rate.

The frequency of collisions with the background gas is proportional to the interaction cross-section and the mean free path of the particles. The mean free path in kinetic gas theory is given by:

$$\lambda_{fp} = \frac{k_B T}{\sqrt{2}\pi P 4a^2}. \tag{3}$$

It is dependent on the pressure P in the volume in question. The scattering rate is given by most probable particle velocity $v_{mp} = \sqrt{\frac{2k_B T}{m}}$ over λ_{fp}:

$$f_{scattering} = \frac{8\pi a^2 P}{\sqrt{k_b T m}}, \tag{4}$$

which is dependent on pressure P particle radius a and temperature T, as well as the mass of the background gas m.

Both short and long wavelength forms of environmental decoherence lead to an increase in particle energy that deviates from the Schrödinger model. This can be exemplified in the time dependent expansion of a minimal uncertainty wave-packet, such as the one of a harmonic oscillator in the ground state:

$$\sigma_s(t) = \sqrt{\frac{\hbar^2 t^2}{4m^2\sigma_0^2} + \sigma_0^2}, \tag{5}$$

where σ_0 is the extension of the minimal uncertainty wave packet at time $t = 0$ and m is the mass of the particle. This term is expanded by a diffusion term of the form $\frac{2\hbar^2 \Lambda t}{3m^2}$, resulting in:

$$\sigma_{dec}(t) = \sqrt{\frac{\hbar^2 t^2}{4m^2\sigma_0^2 2} + \sigma_0^2 + \frac{2\Lambda t^3 \hbar^2}{3m^2}}. \tag{6}$$

This deviation, given by $\sigma_{dec} - \sigma_s$, can be determined experimentally, as a test to decoherence theory as well as to determine the magnitude of blackbody interactions on subwavelength particles. In particular the measurement of the

actual decoherence parameter as a function of temperature will allow the limits they pose to future experiments in the quantum regime to be determined. Necessary experimental parameters for observing this effect will be discussed in the following section.

Experimental Parameters to Observe Blackbody radiation induced Diffusion

To quantify the effect of blackbody radiation induced wave-packet diffusion, the extension of the wave packet needs to be measured and compared to the theoretical prediction. However to distinguish between normal expansion and other effects, such as decoherence, a sufficient measurement sensitivity is necessary. In addition to this, the width of a wave-packet is not an observable [18], thus it is necessary to extract it from the statistical position distribution over many measurements. The magnitude of the decoherence effect, the expansion time and the initial width of the ensemble determine both the required measurement sensitivity, as well as the number of measurements that need to be performed to allow the expansion rates to be distinguished. In an experiment these can be controlled via temperature, pressure and trap frequency. In the following, we will give a short overview of what is necessary to observe the effects of blackbody radiation induced diffusion for feasible experimental values. A deeper analysis for space based experiments can be found in [19].

The difference between accelerated diffusion and standard diffusion, $\sigma_{dec}(t) - \sigma_s(t)$, can be approximated as:

$$\sigma_{dec}(t) - \sigma_s(t) \approx \frac{\Lambda t^3 \hbar^2}{3m^2}, \tag{7}$$

assuming the decoherence term is much smaller than the regular free evolution. The statistical error in estimating the width of the ensemble is given by:

$$\Delta\sigma(t) = \frac{\Delta q}{\sqrt{N-1}}, \tag{8}$$

where Δq is the position measurement error and N the number of measurements. This value has to be smaller than the difference $\sigma_{dec}(t) - \sigma_s(t)$, leading

to the minimum diffusion parameter Λ that can be distinguished being given by:

$$\Lambda_{min} = \frac{3m^2 \Delta q \sigma_s t}{\sqrt{N-1}\hbar^2 t^3}. \tag{9}$$

Given a test particle of radius 150nm with a free evolution time of 10ms, 100 measurements with a 10pm precision can at best distinguish a diffusion parameter of $\Lambda \approx 10^{23} m^2 s^{-1}$. While this overestimates the error in position measurement, it makes clear that the number of performed measurements is vital to get a precise estimation of the ensemble width.

To observe blackbody radiation induced diffusion it is possible to either increase the blackbody contribution to be larger than the one of background gas scattering and perform longer freefall measurements, or to perform measurements on timescales where on average no gas scattering occurs. Both of these methods require extremely low pressures.

Fig.1 plots the gas scattering diffusion and the blackbody diffusion as a function of temperature with a particle radius of 150nm. At a pressure of 10^{-11} mBar, a value that should be experimentally achievable in a dedicated UHV system, an external temperature of 1400K is necessary for blackbody induced recoil to surpass gas scattering. This temperature is also the break even point to observe Λ_{min} from blackbody interactions alone.

An experiment that aims to evaluate the magnitude of blackbody effects on subwavelength therefore has multiple requirements:

- Ultralow pressures, to minimize gas scattering rates.
- High temperatures, exceeding 1400K, to achieve an observable effect due to blackbody radiation.
- Large number of experimental repetitions, to determine the ensemble width with minimal statistical error.

Additional requirements are cooling the motion of the test particle close to the ground state and the capability to recapture the particles after the free evolution, to measure their position. All these requirements demand additional

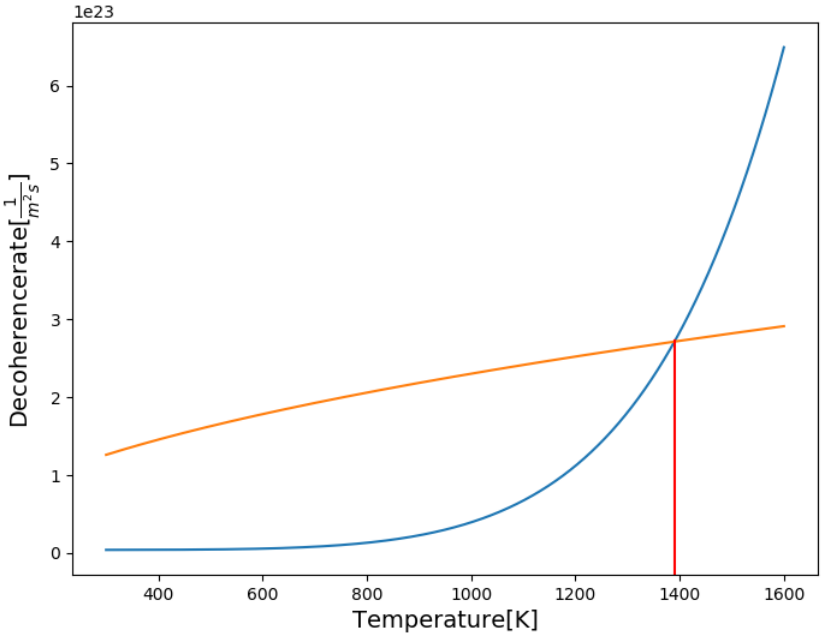

Figure 1: Temperature dependence of blackbody Λ_{bb} (blue) and gas scattering Λ_{air} (orange) diffusion rates. This graph shows the dependence of diffusion rates for a particle of radius $a = 150$nm at a pressure of $P = 10^{-11}$mBar. The decoherence parameter Λ_{bb}, which scales with a^6, surpasses the contribution from gas scattering at around 1400K (red line).

development of technology to be implemented in an optomechanical setup. In particular, the crucial upgrades that are needed are a method to load test particles into the ultrahigh vacuum environment and a measure to recapture them reliably after a free fall. The necessary experimental parameters to observe the effect on blackbody radiation on the diffusion of the wavefunction are summed up in Table I.

In the following we introduce an experimental setup, that should allow the measurement of blackbody induced wave-packet diffusion.

Experimental Proposal

An experiment with the goal of quantifying blackbody decoherence is a challenging undertaking. To perform freefall experiments with particles cooled to

P_{max}	T	a	N	Δ q	$f_{particle}$
$<10^{-11}$mBar	$>$ 1400K	150nm	100	10pm	100kHz

Table I: Experimental parameters required for the observation of blackbody radiation induced wave packet diffusion. At a pressure of 10^{-11}mBar a free evolution time of up to 10ms can be achieved for a particle with radius a =150nm. Performing N=100 free fall measurements at 1400K should allow the effect of blackbody diffusion to become observable.

the ground state, optimal motion detection and control is required, as well as a mobile trap capable of recapturing particles to measure their position. Additionally an optimal experiment needs to lower the pressure far enough that on average no gas scattering occurs during an experimental run.

Fig.2 shows a proposed experimental setup that can reach 10^{-11} mbar in pressure, by using a combination of turbo molecular, ion and non evaporative getter pumps. Such a combination of pumps can reliably reach even XHV pressures [20] under optimal conditions. This will allow for ms free fall times to be achieved and for blackbody induced diffusion to surpass gas scattering terms at temperatures exceeding 1400K.

To enable free fall experiments a two-axis acousto optic deflector (AOD) will be used for beam scanning in 2D. With this configuration the tweezer position can be scanned over several hundreds of μm. In addition to this, one can create multiple traps using this configuration [21], allowing arrays of particles to be loaded into the UHV chamber.

The particles can be recaptured after free fall, by creating another trap at a set distance and time. A closer look at a proposal for the experimental setup in the chamber can be seen in Fig.3. This design will include a hollow-core fiber optical conveyor belt, to load particles into the optical tweezer at UHV pressures. In addition a particle trapped in the optical tweezer can be heated using a tungsten heating element capable of reaching over 1500 K, which allows a blackbody diffusion rate Λ_{bb} of over $10^{23}\mathrm{m}^2\mathrm{s}^{-1}$ to be reached, surpassing

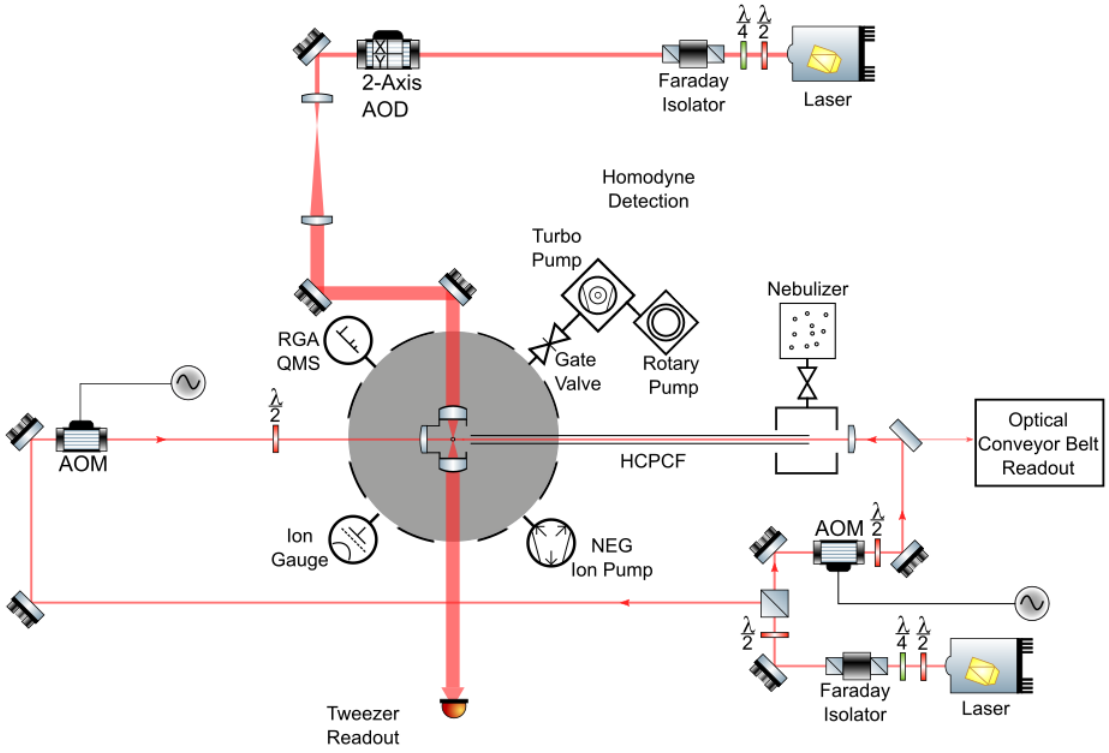

Figure 2: Plan for an experimental setup to probe blackbody radiation induced wave packet diffusion. The system is designed to provide the necessary parameters to observe blackbody induced diffusion. To achieve the required pressure of 10^{-11} mBar a combination of turbopump, iongetter and non evaporative getter pump is used. Using a cathode heater temperatures exceeding 1500K can be achieved, to enhance the effects of blackbody diffusion to an observable level. Finally the setup is equipped with a 2 axis AOD to allow a movable tweezer trap in 2D. Multiple traps can be generated and moved in this fashion [21], allowing for recapture of particles after freefall. Particle loading will use an improved hollow-core fiber transfer system.

contributions of gas scattering at the desired pressure. This temperature is still far from the melting point, approximately 1900K, of SiO_2

This temperature is sufficient to achieve a decoherence parameter and should therefore allow the experimental observation of the accelerated spread of the wave-packet.

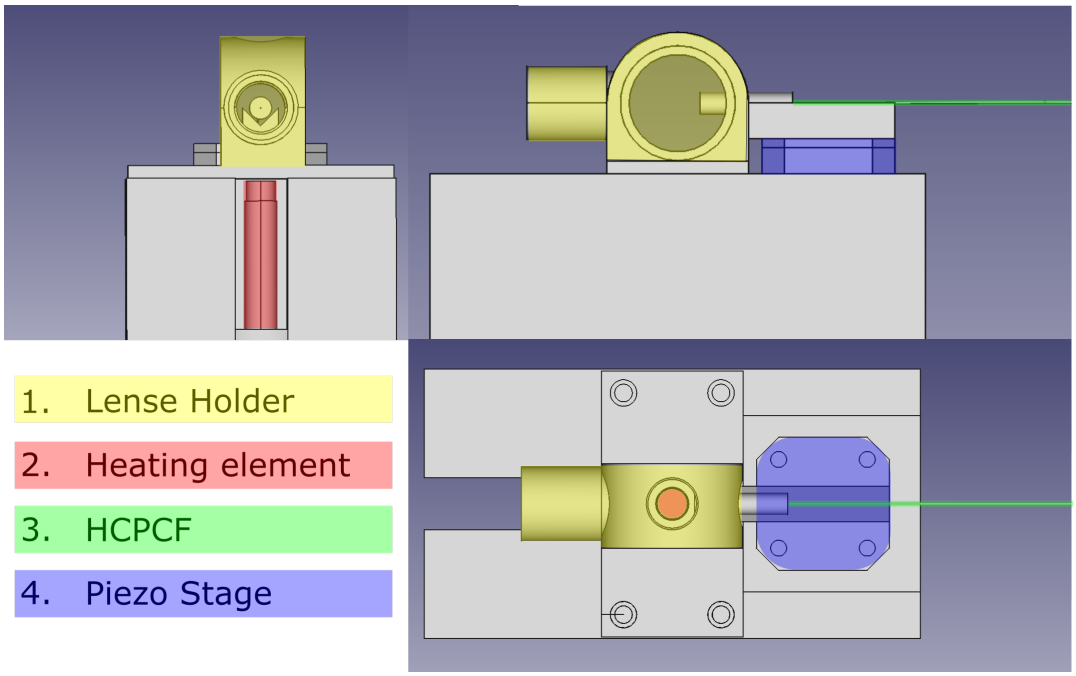

Figure 3: CAD Design of the core experiment to observe blackbody diffusion effects. Two identical aspheric lenses will set up a tweezer trap and collect the outgoing light for detection. To generate the temperature required for the experiment, a heating element capable of reaching above 1500K is placed underneath the tweezer. This should allow the required diffusion rate to be achieved. Particle loading will take place via a hollow-core photonic crystal fiber mounted onto a 3D piezo stage, to allow for repeatable alignment.

Summary

In conclusion, this chapter introduced the concept of environmental decoherence, how blackbody radiation contributes to wave-packet diffusion and how this deviation from Schrödinger's theory can be experimentally verified. We proposed a setup that, once the technical challenges are overcome, can allow the measurement of these effects. This will serve to deepen our understanding of the limits macroscopic quantum experiments will be subjected to due to unavoidable blackbody interactions.

PRINCIPLES OF OPTICAL LEVITATION

Since Arthur Ashkin first used optical forces to trap dielectric particles [22] [23] [24], the use of optical traps has found a wide range of application [25]. Of the different type of traps the one relevant in this thesis is the single beam gradient force trap, referred to as an optical tweezer. This section will cover the necessary basics for optical levitation of sub-wavelength scale particles in gaussian beams, as well as present the basics necessary to understand standing wave traps and optical conveyor belts.

Gaussian Beams

The fundamental TEM00 mode profile of a gaussian beam, with wavelength λ and frequency ν, that is propagating along in the z direction has the following EM field equation:

$$\vec{E}(x,y,z) = E_0 \frac{w_0}{w(z)} e^{-\frac{x^2+y^2}{2w^2}} e^{-ik\frac{x^2+y^2}{2R(z)}} e^{-i(kz-\zeta(z))}, \tag{10}$$

where $w(z) = w_0\sqrt{1+\frac{z}{z_R}}$ is the beam waist at distance z from the minimal waist w_0. $z_R = \frac{\pi w_0^2}{\lambda}$ is the Rayleigh length and $k = \frac{2\pi}{\lambda}$ is the wave number. $R(z) = z(1+\frac{z_R^2}{z^2})$ is the wavefront curvature and $\zeta = \arctan(\frac{z}{z_R})$ is the Gouy phase. The time averaged intensity distribution of such a beam is given by:

$$I(x,y,z) = \frac{2P}{\pi w(z)^2} e^{-\frac{x^2+y^2}{w(z)^2}}, \tag{11}$$

where the power, $P = \frac{1}{4}\pi\epsilon_0 c w_0 n_2 E_0^2$, is taken from [26]. In the paraxial approximation the relation between the beam waists at the focus and before the focussing lens is given by:

$$w_0 = \frac{\lambda f}{\pi w_{in}}, \tag{12}$$

where f is the focal length of the lens and w_{in} is the beam waist of the incoming beam. As this relation follows from using the paraxial approximation it does does not hold for tightly focused gaussian beams [27]. However, for

the purposes of this thesis it is a sufficient approximation for the implemented experiment.

Standing waves

Standing waves, such as the one used for transporting particles in this thesis, are generated by superimposing two coherent counter propagating beams with matching polarization. For two gaussian beams with equal amplitudes $E = |\vec{E_1}| = |\vec{E_2}|$ and waist w the intensity is proportional to:

$$I(r,z) \propto E^2 \frac{w_0^2}{w(z)^2} e^{\frac{-r^2}{w^2(z)}} 4\cos^2\left[k(z+\frac{r^2}{2R(z)})\right], \tag{13}$$

which is given by the superposition of the electric field amplitudes. For $R(z) >> r$ the second term of the cosine function can be neglected and the intensity reduces to:

$$I(r,z) = \frac{8P}{\pi w(z)^2} e^{\frac{-r^2}{w^2(z)}} \cos^2(kz). \tag{14}$$

The intensity distribution along the propagation axis can be seen in Fig.4.

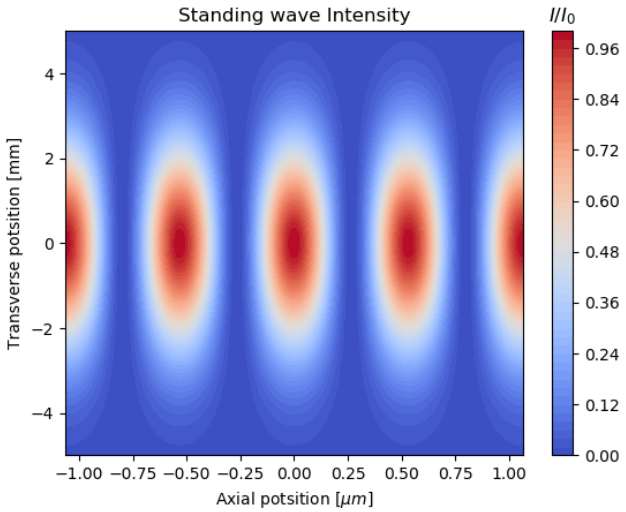

Figure 4: Intensity distribution of a collimated standing wave beam along the propagation axis with a wavelength of 1064nm.

In this thesis the standing wave is generated by coupling counterpropagating beams into a hollow-core fiber with waist radius of $w = 3.35 \pm 0.5\mu$m. As

coupling losses are unavoidable equal power inside of the hollow-core fiber will lead to an unbalanced power outside of the fiber, as the incoming beam will have higher power than the one leaving the fiber. The intensity of the unbalanced standing wave can be expressed with:

$$I(r,z) = \frac{4P}{\pi w(z)^2} e^{\frac{-r^2}{w^2(z)}} \left(\frac{1+\eta^2}{2} + \eta \cos(2kz) \right), \tag{15}$$

where $\eta^2 = \frac{P_{high}}{P_{low}}$ is the ratio between the optical powers. Due to this the intensity varies between the extremes of $I_{max} = \frac{4P}{\pi w(z)^2} \frac{(1+\eta)^2}{2}$ and $I_{min} = \frac{4P}{\pi w(z)^2} \frac{(1-\eta)^2}{2}$

Optical Forces

A small dielectric particle in the Rayleigh regime ($a \ll \lambda$), such as the ones used in the experiment, mainly experiences two forces while interacting with an electromagnetic field. In this regime the particle can be treated as a point-like dipole, which is polarized by the electromagnetic field. This dipole scatters the incoming light, emitting it as dipole radiation. The absorption and scattering of incoming photons imparts a momentum on the nanoparticle, which is described by the scattering force $\vec{F}_{scatt}$. The force takes the form:

$$\vec{F}_{scatt}(r,z) = \frac{\sigma_{scatt}}{c} I(r,z) \vec{e}_z, \tag{16}$$

where $\sigma_{scatt} = \frac{8}{3}\pi k^4 a^6 \frac{(\epsilon-1)^2}{(\epsilon+1)^2}$ is the scattering crosssection of the dielectric Rayleigh particle, a its radius and ϵ its dielectric constant.

In addition to this nonconservative scattering force, the gradient force $\vec{F}_{grad}$ acts on the particle pulling it to intensity maxima. The force is given by:

$$\vec{F}_{grad}(r,z) = \frac{\alpha}{2\epsilon_0 c} \nabla I(r,z), \tag{17}$$

with polarizability $\alpha = 4\pi\epsilon_0 a^3 \frac{\epsilon-1}{\epsilon+2}$. The polarizability and therefore the gradient force is proportional to the volume of the particle. As the gradient force is conservative we can find a potential, which takes the form:

$$U(r,z) = -\frac{\alpha}{2\epsilon_0 c} I(r,z). \tag{18}$$

One of the optical traps used in this thesis is the single beam optical tweezer. In such a trap a particle is held in a tightly focused gaussian beam. The optical potential, neglecting the scattering force, is then:

$$U(x,y,z) = -\frac{2P\alpha}{w^2(z)\pi\epsilon_0 c} e^{-\frac{x^2+y^2}{w^2(z)}}. \tag{19}$$

The motion of a particle trapped in an optical tweezer is usually confined to small displacements from the trap center. In this case the potential can be expanded in a Taylor series, breaking of after the quadratic term, which results in the harmonic approximation:

$$U(x,y,z) \approx U(0) + \sum_i \frac{\partial U(x,y,z)}{\partial x_i}\Big|_{x,y,z=0} x_i + \sum_i \frac{\partial^2 U(x,y,z)}{\partial^2 x_i}\Big|_{x,y,z=0} x_i^2 + \mathcal{O}(x^4). \tag{20}$$

The spring constant for each direction of motion is given by the factor for the quadratic term $\kappa_i = \frac{\partial^2 U(x,y,z)}{\partial^2 x_i}$. From these the trap frequencies attributed to each direction is $\Omega_i = \sqrt{\frac{\kappa_i}{m}}$, where m is the mass of our particle. The radial trap frequencies in a single beam trap are given by:

$$\Omega_{x,y}^2 = \frac{4P\alpha}{\pi m c \epsilon_0 w_0^4} \tag{21}$$

and are independent of particle size, as both polarizability α and mass of the particle scale with its volume. Along the axial direction the trap frequency is given by:

$$\Omega_z^2 = \frac{4P\alpha}{\pi m c \epsilon_0 w_0^2 z_R^2}. \tag{22}$$

Since the gradient force is conservative it is not capable of capturing and stopping particles moving through the trap on its own. A particle that moves through the potential gains enough kinetic energy to leave it. Either a mechanism of energy dissipation or a way to deliver the particle without it interacting with the entire potential is necessary for capturing a particle that falls into the conservative potential. Conventionally trapping occurs at high pressures, such that gas damping provides the necessary friction. The gas damping follows the approximation [28]:

$$\gamma_{gas} = \frac{6\pi\mu a}{m} \frac{0.619}{0.619 + Kn}(1 + c_K), \tag{23}$$

where μ is the viscosity of the gas medium, $c_K = \frac{0.31Kn}{0.785+1.153Kn+Kn^2}$ a high pressure correction factor, $Kn = \frac{\lambda_{fp}}{a}$ the Knudsen number and λ_{fp} the mean free path. Using this damping the motion of a trapped dielectric nanosphere can be expressed with a dampened harmonic oscillator:

$$\ddot{x} + \gamma\dot{x} + \Omega^2\kappa x = \frac{F_t}{m}, \tag{24}$$

where F_t is the thermal force noise introduced by scattering of background gas. To express it in one dimension we used the fact that the motion along the different axes do not influence one another.

The motion and trajectory of the particle in the trap can be used to determine the trap properties, such as damping, frequency and waist. This is typically done via the spectrum of particle motion, given by:

$$S_{xx}(\omega) = \left\langle \left|\tilde{x}(\omega)\right|^2 \right\rangle \tag{25}$$

where $\tilde{x}(\omega) = \frac{2k_BT\gamma}{m[(\Omega^2-\omega)^2+\omega^2\gamma^2]}$ is the displacement in Fourier space.

Standing wave traps

A standing wave, such as introduced before, can also serve as an optical trap. Such a trap works in much the same way as a single beam trap, as subwavelength particles are trapped via the gradient force. The major difference between the traps is the shape of the optical potential. Additionally, the scattering force contribution can be cancelled in a standing wave trap, if equal optical power is used in the two counterpropagating beams. The potential takes the form:

$$U(x,y,z) = -\frac{4P_{SW}\alpha}{\pi\epsilon_0 c w_{SW}^2(z)} e^{-\frac{x^2+y^2}{w_{SW}^2(z)}} \left(\frac{1+\eta^2}{2} + \eta\cos(2kz)\right), \tag{26}$$

where P_{SW} and w_{SW} are the optical power in the standing wave, as well as the beam waist. A Rayleigh particle trapped in a standing wave is more confined along the propagation axis, compared to a single beam trap, as the interference maxima occur at $\lambda/2$ distance. Once again the motion can be harmonically

approximated, as in .

From the harmonic potential one can again determine trap frequencies. The axial trap frequency is then given by:

$$\Omega_{z,STW}^2 = \frac{8\alpha P_{SW}}{c\pi\epsilon_0 m w_0^2}\left(\frac{1}{z_R^2} + 2k^2.\right), \tag{27}$$

which, for equal power, is higher compared to the single beam trap.

The radial frequency follows:

$$\Omega_{r,STW}^2 = \frac{8\alpha P_{SW}}{c\pi\epsilon_0 m}\frac{1}{w_0^4} \tag{28}$$

which is notably just twice that of the single beam trap, as the power is doubled. For unbalanced beams the power ratio η^2 flows into the motional frequencies giving:

$$\Omega_{z,STW}^2 = \frac{8\alpha P}{c\pi\epsilon_0 m w_0^2}\left(\frac{(1+\eta)^2}{2z_R^2} + \eta 2k^2\right), \tag{29}$$

for the axial frequency and:

$$\Omega_{r,STW}^2 = \frac{4\alpha P}{c\pi\epsilon_0 m}\frac{(1+\eta)^2}{w_0^4}, \tag{30}$$

for the radial frequencies.

Particle Transport

The attributes of a standing wave trap can be exploited to move particles along the propagation axis of the beam. As particles are confined to a single intensity maximum they will move along with the intensity maxima when they are shifted along the beam axis. The effects of a change in path length or a detuning in frequency can be included in the cosine term of the intensity distribution:

$$I \propto |e^{i(kz-2\pi\nu t} + e^{i(k(z+\frac{z_0}{2})+2\pi(\nu-\Delta)t}|^2 = 1 + \cos(2k(z - \frac{z_0}{2}) + \pi\delta t), \tag{31}$$

once again neglecting the curvature term. Here we introduced a frequency detuning term Δ as well as a path length difference z_0. These represent the two ways the intensity maxima are shifted in this thesis.

For example by moving a mirror a distance z_0, the optical path length in one beam changes by a distance of $2z_0$. This leads to a change in position of the particle in its intensity maximum by z_0.

The other transport mechanism is achieved by detuning the frequency of one beam with respect to the other. This leads a motion of the intensity maxima at a constant velocity, creating what is known as an optical conveyor belt [29]. The speed with which the conveyor belt moves is proportional to the detuning. It follows:

$$v = \frac{dz}{dt} \approx \frac{\pi\Delta}{k} = \frac{\lambda\Delta}{2}. \tag{32}$$

For a wavelength of λ =1064nm and a detuning of 1kHz this would result in a conveyor belt velocity of $\approx 532\mu m/s$.

Overlapping traps

In this thesis a combination of standing wave trap and single beam trap are used. Fig.5 shows the optical potentials generated in the tweezer trap, in the standing wave, as well as the combined potential.

The idea behind the transfer is to align the standing wave with the tweezer trap, such that their centres overlap. A particle trapped in the conveyor belt can then be moved into the tweezer trap.

The standing wave trap is generated inside and outside of a hollow-core fiber. A minimal distance between the terminal end of the hollow-core fiber and the tweezer trap is necessary to avoid clipping of the beam and affecting the tweezer trap. The distance is given by the diameter of the fiber and the waist of the tweezer.

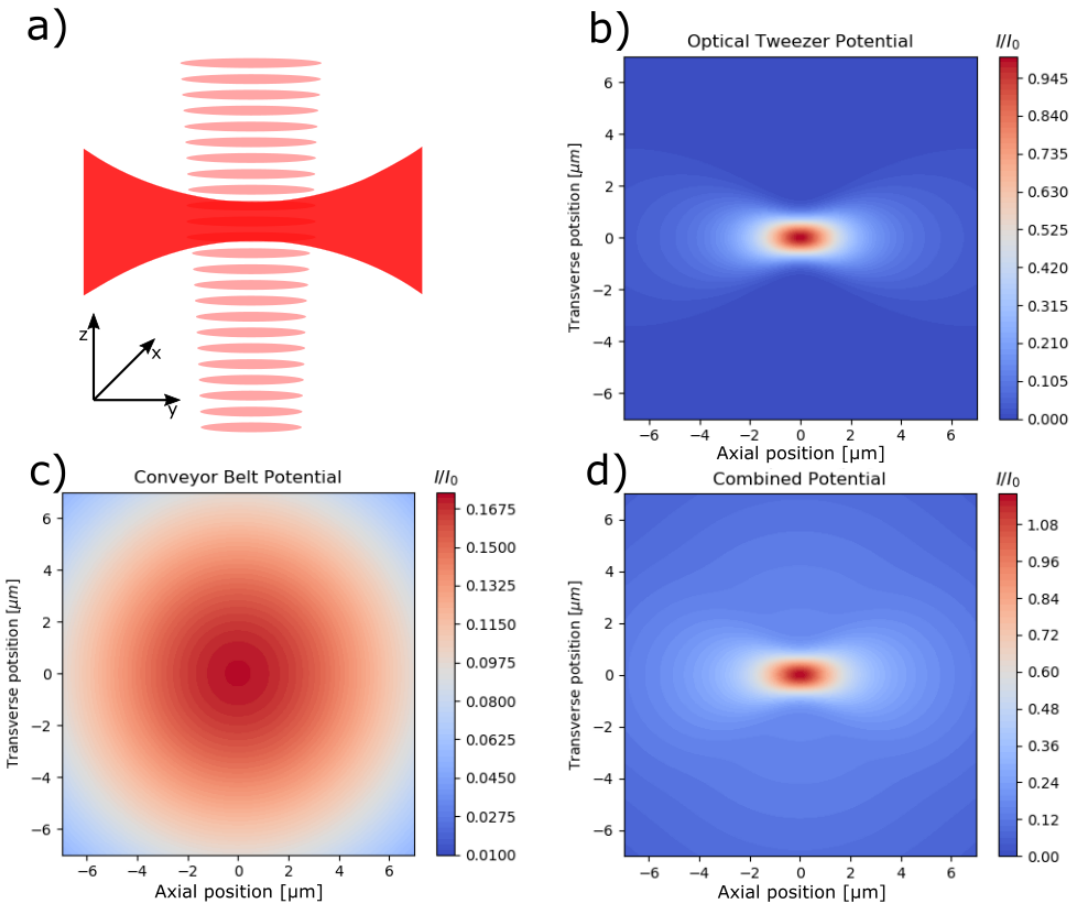

Figure 5: Optical traps relevant in this thesis. a) A standing wave with a diverging beam profile is used as optical conveyor belt to transport particles from a hollow-core fiber to the focus of an optical tweezer, which propagates perpendicular to the conveyor belt (not to scale). b) Contour plot of the intensity distribution at the particle trap position in crosssection for b) the optical tweezer potential and c) the optical conveyor belt (standing wave maximum). d) shows the combined potential in crossection of the tweezer. The contribution to the optical potential due to the conveyor belt is hardly visible. Note the different color scales for the plots, chosen to allow the standing wave to more visible.

For a fiber with a diameter of 125μm the distance between minimal waist and tweezer trap is sufficient for the approximation in Eq. 5 to hold. As

such the total potential the particle experiences is given by the sum of both potentials, $U_{Tw}(x,y,z) + U_{SW}(x,y,z)$:

$$U_{tot} = \frac{-2\alpha}{\pi\epsilon_0 c}\left[\frac{P_1}{w_1^2(z)}e^{-\frac{x^2+y^2}{w_1^2(z)}} + \frac{2P_2}{w_2^2(y+d)}e^{-\frac{-x^2+z^2}{w_2^2(y+d)}}\left(\frac{1+\eta^2}{2} + \eta\cos(2k(y+d))\right)\right], \tag{33}$$

where d is the distance between fiber and tweezer. P_1 and w_1, as well as P_2 and w_2 denote the optical power and beam waist of tweezer and standing wave respectively. A usual value for the power ratio between incoming and outgoing beam in the standing wave trap is $\eta^2 = 1.5$. This is partially due to the coupling losses, with the achieved efficiencies of approximately 70% and due to a purposeful imbalance which aims to increase the trap depth outside of the fiber.

Once again the harmonic approximation can be applied, to evaluate trap frequencies for small displacements. Due to the trap configuration, the frequencies along the three axes are affected differently by the overlap. The frequency along the y-axis, the propagation axis of the standing wave, is given by:

$$\Omega_y^2 = \frac{4\alpha}{\pi m\epsilon_0 c}\left[\frac{P_1}{w_{0,1}^4} + \frac{P_2}{w_2^2(d)}\left(\frac{(1+2\eta\cos(2kd)+\eta^2)}{2z_{R,2}^2} + k^2\eta\cos(2kd)\right)\right], \tag{34}$$

where $w_{2d}(d)$ is the standing wave waist at distance d.

The frequency along the x axis follows:

$$\Omega_x^2 = \frac{4\alpha}{\pi m\epsilon_0 c}\left[\frac{P_1}{w_{0,1}^4} + \frac{P_2(1+2\eta\cos(2kd)+\eta^2)}{2w_2^4(d)}\right]. \tag{35}$$

Finally the frequency along z is:

$$\Omega_z^2 = \frac{4\alpha}{\pi m\epsilon_0 c}\left[\frac{P_1}{w_{0,1}^2 z_{R,1}^2} + \frac{P_2(1+2\eta\cos(2kd)+\eta^2)}{2w_2^4(d)}\right]. \tag{36}$$

Ω_y is affected most strongly by the standing wave potential, as the particle is confined most strongly along this axis by the standing wave. The motion along the other axes is only negligibly affected in comparison, as the large waist of the standing wave weakens the effect. The depth of the overlapping potential is influenced by the distance between fiber and tweezer, as the position of the standing wave maxima is tied to the optical path length. Due to drifts in the

optical path length the intensity maxima will move across the optical tweezer, leading to drifts in frequency.

Summary

This chapter introduced the concept of optical traps and summarized the basic physics behind them. Particle transport along a standing wave trap was introduced, both by frequency detuning and changing the optical path length. We described the potential expected in our experiment for experimental demonstration of particle handover.

STATE-OF-THE-ART

Levitated optomechanics had its revival about a decade ago. Since then, the field has been rapidly growing.

In the following we discuss the state of the art from the perspective relevant to the observation of diffusion by blackbody radiation, i.e. controlling nanoparticles at XUHV vacuum conditions. The major challenge to achieving this today arises from the commonly used methods for loading particles into optical traps. We will briefly summarize existing methods and motivate our choice of using hollow-core photonic crystal fibers.

Optical Levitation and Vacuum

Among the foremost advantages of levitating micro and nanoparticles in optical traps is the achievable decoupling and isolation from the environment. This, along with the capability of precise motional control, allow the probing of very small forces and even to reach the quantum regime of motion. At sufficiently low pressures, $\ll 1$ mBar, the loss of levitated particles was observed [30] [31]. Methods to control the centre of mass (COM) motion of the particle were introduced to cool the particle motion and prevent such losses.

The higher the vacuum level the better the particle is isolated and the lower the gas damping. This corresponds to an increase in gas limited mechanical quality factor Q. This Q factor of levitated micro and nanoparticles can exceed 10^{10} at UHV pressures, following the approximation from [32] for low pressures:

$$Q = \frac{\omega_m}{\gamma_{gas}} \approx \frac{\omega_m \pi \bar{v} \rho a}{16P}, \tag{37}$$

where $\bar{v}$, P, a and ρ are mean gas particle velocity, ambient pressure, particle radius and particle density respectively. The pressure dependence of the mechanical quality factor is one of the reasons why higher vacuum levels are preferred for optical levitation experiments. At high vacuum pressures (below 10^{-5}mBar), which is common in experiments around the world, Q-factors of 10^9 are achievable, which is comparable to other optomechanical systems, such

as membranes or cavities [33] [34] [35].

Optical levitation in UHV

This section aims to give a short overview of state of the art levitation experiments in HV and UHV. Many of the groups working with levitated nano- and microparticles operate in high vacuum pressures of 10^{-8}mBar [36] [37] [38].

The lowest pressure achieved in an optical levitation experiment to date was in [11], an experiment testing the effects of recoil heating on the particle motion. In this experiment, performed in pressures as low as $7*10^{-9}$ mBar, the feedback cooling of a trapped particles was periodically switched and reheating measurements performed. In this fashion, the contribution the COM motional heating of recoil photons was found to be 25 times larger than those due to background gas scattering. This demonstrated, that the limit to optical levitation experiments in this regime is set by the trapping light.

The same setup was used in attempts to reach the motional ground state. In [5] laser shot noise and recoil heating were also identified as the largest constraints to reaching the sub 1 phonon occupation numbers. Reheating of the COM motion by gas scattering still contributed in a small manner, however photon recoil is the greater contribution by a large factor.

The motional ground state was reached at even higher pressures of around 10^{-6}mBar, in [39], where a cavity was used to cool the motion of a particle below single phonon occupation numbers via coherent scattering.

Loading particles into optical traps

To date the base pressure, or the achievable vacuum level, of optical levitation experiments has been limited to high vacuum, with only very few experiments barely reaching UHV. To enable experiments testing the effects of black body radiation it is required to reach these pressures reliably and in a timely fashion.

The main barrier to reaching UHV faced by optical levitation experiments *is surface contamination of the vacuum system* and the resulting high gas load. Such contaminants can be removed by baking the vacuum system at moderately high temperatures , over70°C, for extended periods of time, usually at least 72 hours. In optical levitation experiments however, the contamination of the chamber stems from the loading method employed for the optical trap, meaning the chamber needs to be baked after the loading takes place, which is not experimentally feasible.

For these reasons one needs contamination free loading mechanisms, that are compatible with reaching pressures below 10^{-9}mBar. Usually such methods dessicate the particles before introducing them to the vacuum system and are referred to as "dry-loading techniques". Additionally, designing a loading scheme to allow for direct loading into UHV will allow experiments to bypass lengthy pumping times.

Nebulizer:

The standard method for loading particles into optical traps is by using a nebulizer source. Such a source (e.g. [40]) generates aerosol particles by ultrasonicating a liquid-particle solution. The vapor is then directed into a science chamber at low vacuum pressures. This method allows for a wide range in particle sizes to be delivered to a trap in great numbers. While easy to implement and reliable, the method has a major drawback when viewed under the criteria of ultra high vacuum feasibility. The aerosol droplets adhere to surfaces in the vacuum system and contaminate it. This is especially undesirable in experiments containing high finesse cavities, as these can be adversely affected by the contaminants.

Loudspeaker Source:

An alternative to the nebulizer source is given by the piezo speaker source. Since Arthur Ashkin first used piezo shakers to load particles into optical traps several variations of piezo speaker sources were developed [41] [42]. One such,

used in [43], consists of a microscope cover slide that is clamped to a piezo actuator, an example of which can be seen in Fig.6. Particles suspended in an alcohol solution are poured onto the slide, which is then dessicated. Once dry the particle source can be installed in the vacuum system above the trap.

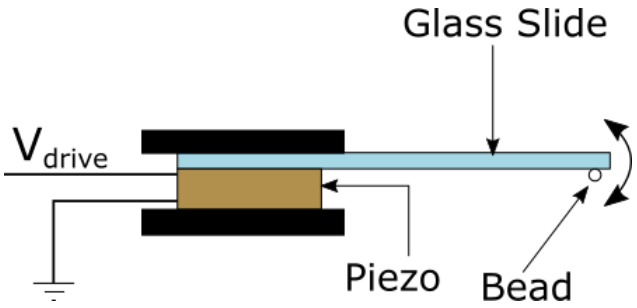

Figure 6: Schematic example of a piezo speaker source. By driving the piezo actuator at resonant frequencies, the particles stuck to the microscope slide can overcome the van der Waals force and fall towards an optical trap.

By driving the piezo crystal at a resonance frequency using an AC voltage the particles are accelerated sufficiently to overcome van der Waals forces holding them to the surface of the microscope slide and knock them towards the trap. As the stiction forces that need to be overcome scale with surface area, only certain particle sizes can be successfully loaded in this fashion. The acceleration required to overcome this force is given by [44]:

$$a_{min} = \frac{3\gamma_{su}}{\rho a^2}, \tag{38}$$

where γ_{su} is the effective surface energy, ρ the particle density and a the radius. For a sphere of radius $a = 150$nm an acceleration of $a_{min} > 8 * 10^8 ms^{-2}$ would be required.

Laser Induced Acoustic Desorption:

Smaller particles can be desorbed from a surface by using laser induced acoustic desorption, or LIAD, introduced in [45] as a molecule source. Particles are smeared on a thin (10-20 μm) metal foil and dried. The foil is then placed in proximity to the trap. By focussing a pulsed laser on the backside of the foil acoustic waves are generated, launching particles in the direction of the trap.

An advantage of this method over a piezo actuator is that much smaller particles can be ejected from the surface. The challenge LIAD faces is the reliance on higher pressures for successful trapping of particles. Particularly in higher vacuum levels the particles cannot be trapped without additions to the mechanism.

In [46], seen in Fig.7, LIAD is combined with timed switching of a Paul trap to demonstrate pressure independent loading. This bypasses the need of a damping mechanism and allows for loading independent of ambient pressure.

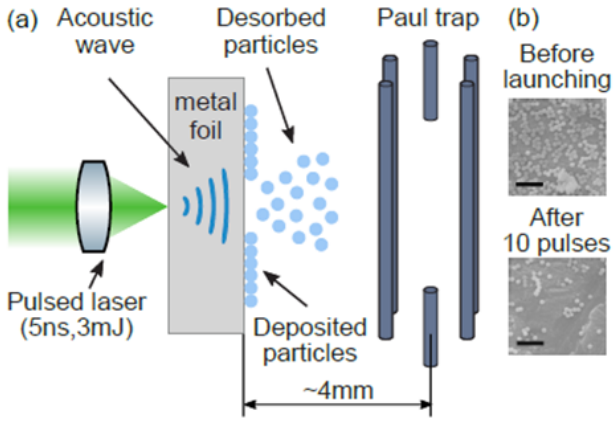

Figure 7: This image, taken from [46], schematically shows the configuration used to load a Paul trap independent from pressure. A set time after particles are ejected from the metal foil by the green laser the Paul trap activates. The particle velocity can be controlled by pulse intensity, which together with variation of the switching time allows for high loading efficiency.

However the current configuration has not been tested for optical traps, which have small trap volumes and depths compared to Paul traps. Using a Paul trap and charged particles places constraints on the experimental design.

Mobile Optical Trap (MobOT):

In order to still use the reliable method of wet loading, one can separate loading and science chamber, as in [47]. There, a mobile optical trap, MobOT for short, is used to prevent the contamination of the science chamber by separating it from the loading chamber. Particles are captured in an optical fiber trap

inside the loading chamber and then moved into an evacuated, clean science chamber, before being deposited in the experiment proper. This method was used to load partices into an optical cavity at pressures of 10^{-5} mBar. While lower pressures can be reached, the pressure during transfer will be limited by the base pressure of the loading chamber. Additionally the requirement for a moving tweezer over long distances and two vacuum chambers limits the time efficiency of this method and leaves it comparatively bulky to other in-chamber solutions.

Loading using hollow-core photonic crystal fibers:
By confining an optical conveyor belt to a hollow-core photonic crystal fiber (HCPCF), short hollow-core fiber, loading and science chamber can be separated, see Fig.8 and the science chamber kept clean during loading. Particles can be transported through the hollow-core fiber over long distances and pressure gradients, even allowing the possibility of loading directly into ultra high vacuum.

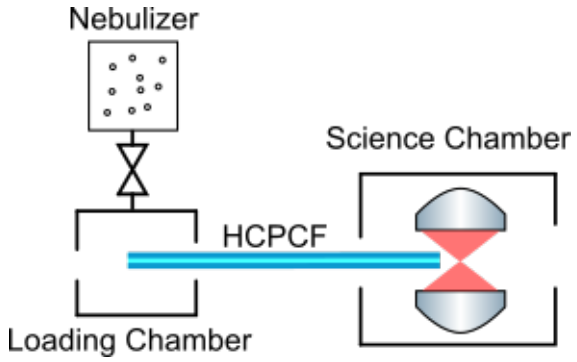

Figure 8: Example of a hollow-core fiber loading scheme for an optical tweezer. Loading and science chamber are connected via the fiber. By loading particles onto the optical conveyor belt in the loading chamber they can be directly transported into the science chamber and deposited in an experiment.

The first use of hollow core fibers in particle transport was for cold atom clouds [48]. From there hollow-core fiber traps in air and liquid for micro [49] and nanoparticles were developed. This thesis expands and is based on work

performed in the Phd thesis of David Grass [50]. The method proposed there is loading particles into optical traps and cavities using an optical conveyor belt, confined to a hollow core photonic crystal fiber.

Hollow core Fibers

In this thesis hollow-core fibers are used in order to allow transport of nanoparticles in an optical conveyor belt over long distances. The underlying principle of these fibers is explained here. In contrast to conventional fibers hollow-core photonic crystal fibers (HCPCF), also known as hollow-core photonic bandgap fibers (HC-PBF) or hollow-core fiber (HCF), do not guide light through the fiber core by total internal reflection, but by relying on a bandgap structure in a photonic crystal surrounding the core.

These fibers can exhibit a variety of properties depending on the design of the photonic crystal cladding, which are covered in [51]. One of the more important properties, for the purposes of this thesis, is the birefringence of the fiber. While a perfectly symmetric core and photonic crystal configuration would not give rise to birefringence in the fiber, even small distortions will result in some birefringence due to the large air-glass index of the core. The fibers used in this thesis are birefringent, which means that for generating a stable standing wave it is necessary to match the polarization angle with the optical axis, to prevent the polarization from rotating.

In Fig.9 such a fiber can be seen, the hollow core surrounded by the photonic crystal cladding, which in turn is covered by a silica mantle.

Here the photonic crystal around the core is illuminated with white light. One can gauge the quality of the cleave and the fiber using this method, as dark spots in the crystal indicate an uneven cleave or contamination of the photonic crystal. An even cleave without shadows, such as the one in Fig.9, allows for coupling efficiencies above 70%, which is sufficient for the procedure performed in this thesis.

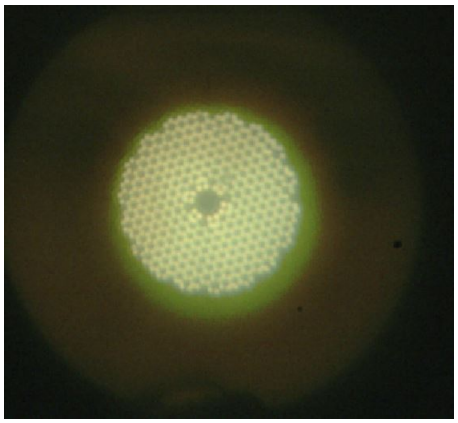

Figure 9: Microscope view of a hollow-core fiber after manual cleaving. The lack of shadows on the photonic crystal and evenness of the cleave indicate a clean fiber.

Hollow-core fibers present themselves as the preferred choice for loading particles into UHV pressures due to the capability of not only dry, but direct loading, which does not face hard constraints in particle size such as piezo catapults.

Summary

The addition of a positioning stage to the fiber loading scheme, as well as the alignment method covered in this thesis, allows the hollow-core fiber in the science chamber to be aligned with respect to a cavity or optical tweezer. This allows deterministic loading of particles into optical traps. One of the main concerns to take into account when connecting two vacuum chambers with different pressure regimes, is how this affects the base pressure of the science chamber, as the loading system effectively introduces a small leak. The question of how many orders of magnitude in pressure can be bridged with such a fiber was addressed in [50] and [52]. It was shown that a hollow-core fiber does not limit the base pressure if the length of the fiber and the core diameter result in a sufficiently small conductance. The maximal pressure difference between high and low pressure regions connected via a hollow-core fiber were compared for fibers of different core diameters. Depending on the

length of the fiber a conductance as low as $C \approx 10^{-10} ls^{-1}$ can be achieved, allowing orders of magnitude in pressure to be bridged by the fiber connection.

In this thesis we experimentally demonstrate the handover of a silica nanosphere between a movable optical conveyor belt and a fixed optical tweezer trap. The demonstration of such a handover at mBar pressures is a crucial step towards later realization in UHV pressures.

EXPERIMENTAL SETUP FOR TRANSFER VIA HOLLOW-CORE FIBER

In this chapter, an experimental setup for the transfer of particles between optical tweezer and optical conveyor belt is demonstrated. It can be subdivided into three parts, namely the optical tweezer trap, the hollow-core fiber trap and the vacuum setup in which both are installed. As the hollow-core fiber trap requires a more complex beam preparation, it is separated into beam launch and fiber trap setups.

Optical Tweezer

The optical tweezer setup, which can be seen in Fig.10, is powered by a 1064nm Keopsys 2W CW fiber-amplifier, that is seeded with 5mW from a 2W Coherent: Mephisto solid state laser. The output of the amplifier is sent through a Faraday isolator to prevent back reflections from damaging the device.

The laser light then passes a $\frac{\lambda}{2}$ waveplate and polarizing beam splitter (PBS), which allow manual control of the optical power directed towards the tweezer. Following this a telescope is used to increase mode matching to the single mode fiber (Thorlabs HI-1060). The reason for this is that the output of the fiber-amplifier (Thorlabs Pandas PM980-XP) has a slightly different mode field diameter for 1064nm light.
To compensate for the polarization rotation induced by the single mode fiber a $\frac{\lambda}{2}$ and a $\frac{\lambda}{4}$ plate are placed after the telescope. The fiber acts as a mode filter before the tweezer.

At the output of the fiber the light is directed through another $\frac{\lambda}{2}$ plate to change the polarization angle of the beam. This allows control of the direction in which the particle emits the dipole radiation, enhancing its visibility on the CCD camera. To achieve a minimal focal waist after the trapping lens the light is expanded in a telescope. Using a pair of lenses with 30mm and 125mm focal length respectively a magnification of 4.167 is achieved. The resulting

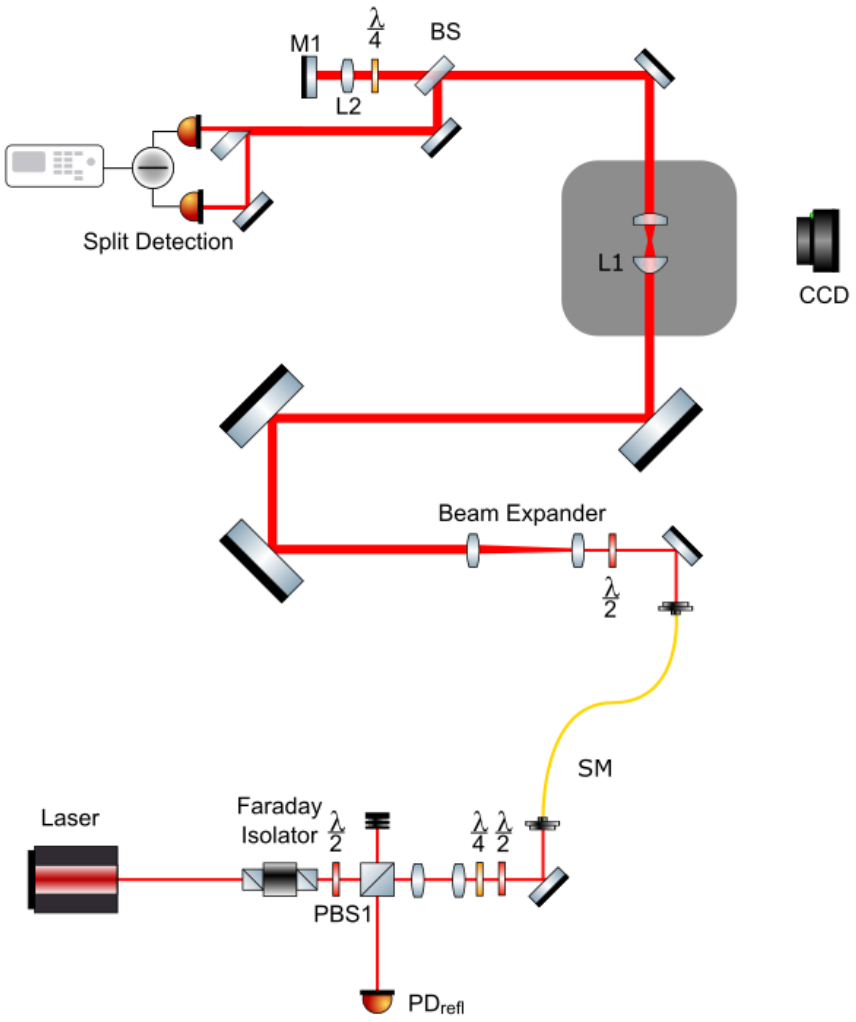

Figure 10: Schematic drawing of the optical tweezer setup. The 1064nm laser source is routed through a PBS and a beam expanding telescope, to be then coupled into a single mode fiber (SM). To compensate for polarization rotations in the fiber a pair of $\frac{\lambda}{2}$ and $\frac{\lambda}{4}$ are placed before the fiber port. The light leaving the fiber is expanded in a telescope to completely fill the trapping lens. After the tweezer the light is split into detection and reflection arms with a ration of 1:9. A split photodiode is used to generate a difference signal, evaluating the particle motion. The beam is reflected by focussing it onto a mirror by using a lens mounted on a translation stage. By tilting the mounted mirror the light is coupled back into the single mode fiber.

beam waist of 5.17±0.03 mm slightly underfills the trapping lens aperture of

11.2mm. The measurement of the beam waist before the tweezer can be seen in Fig.11.

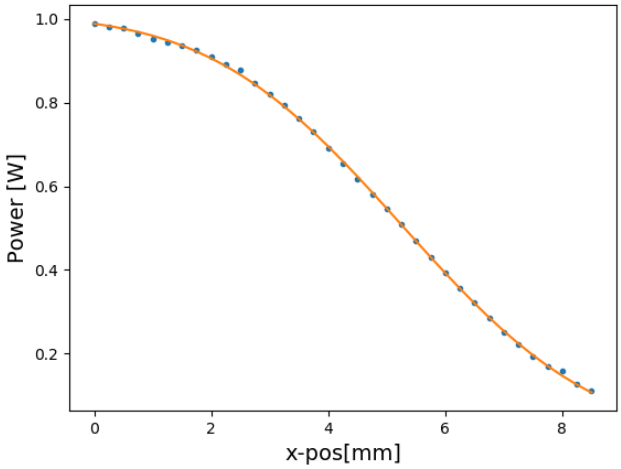

Figure 11: Beam waist measurement of trapping beam after expanding telescope. The beam waist was measured by using a knife edge to block increasing portions of the beam. By fitting the data with an error function the beam waist of 5.17±0.03 mm was extracted.

In this experiment a high numerical aperture (0.8) aspheric lens (L1) [53] is used to focus the beam to generate the optical dipole trap. Compared to a microscope objective with comparable numerical aperture a single trapping lens has several advantages. Especially from the perspective of levitation in UHV a microscope objective is problematic, as the housing could become a virtual leak and the increased surface area and material contribute to outgassing.

After the tweezer trap the light is re-collimated using a 25.4mm focal length lens (Thorlabs LA1951 - N-BK7, NA $\approx$ 0.45). The NA mismatch results in losses in the remaining beam, as the more strongly diverging parts cannot be collected with the lens. Outside of the vacuum chamber the beam is directed towards a 90:10 beamsplitter (Thorlabs BSF10-C).
The 10% in reflection are used for detecting the transverse particle motion in a split detection scheme. The beam is bisected horizontally by utilizing a D-

shaped mirror. This is done so both components can be focused into separate inputs of a split photo diode (Thorlabs: PDB420C-AC), where the difference of both signals gives information on the particle motion. The signal is observed using an oscilloscope (Picoscope 4000) as Spectrum analyzer, displaying the power spectral density of the particle motion in 1 axis, as sensitivity to motion along the fiber axis is increased by splitting the beam along this direction. Due to imperfections the other axes of motion are also visible in the detection. The remaining 90% of the beam are used to create a counterpropagating, orthogonally polarized beam in the tweezer trap, which serves to partially compensate the scattering force along the tweezer axis. For this purpose the light is focused onto a mirror (M1) using a 7.5mm plano-convex lens (L2). In addition a $\frac{\lambda}{4}$ plate is set in double pass, which allows switching between standingwave and non-standingwave configuration in the tweezer by switching polarization. The mirror is mounted on a piezo ring chip (Thorlabs PA44LEW), which allows particle transport along the tweezer axis, by changing the optical path length in the back reflected beam.

To align the reflected beam it is coupled back into the single mode fiber, while being orthogonally polarized to the incoming light. By doing this a reflected signal can be measured using a power sensor at the PD_{down} output of PBS1. The coupling efficiency is maximized by moving L2, as well as changing the orientation of the mirror, which optimizes the alignment of the reflected beam with the tweezer.

Hollow-core fiber Trap

The optical conveyor belt traps particles in the loading chamber and transports them through the hollow-core fiber into the science chamber. This is achieved by setting relative detuning between the counterpropagating beams. It consists of two parts, the beam launch, where the beams are prepared and the fiber trap setup, where the standing wave trap is generated in the hollow-core fiber connecting the two chambers.

The beam preparation of the experiment can be seen in Fig.12. The output

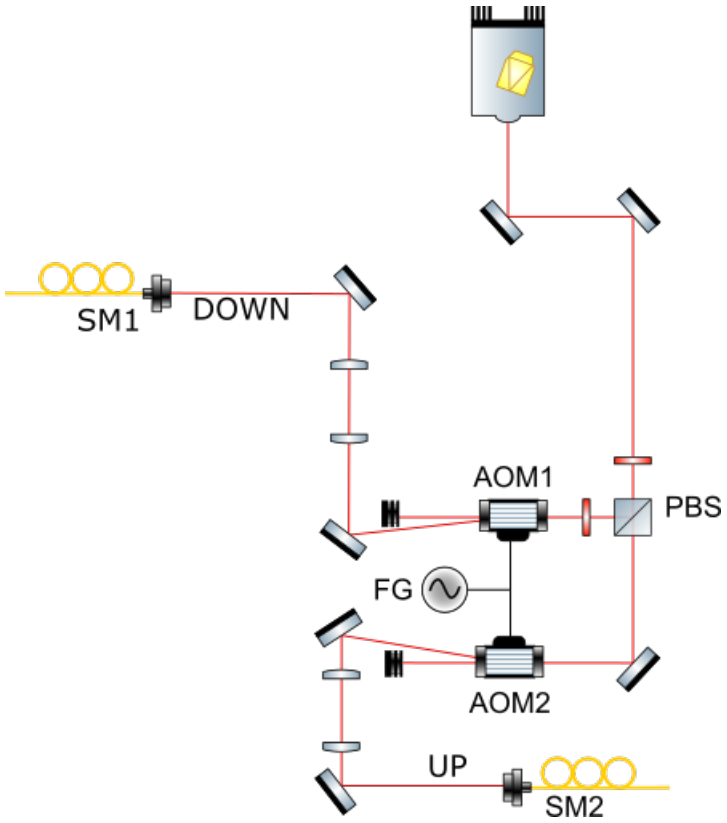

Figure 12: Schematic representation of the laser preparation for the hollow-core fiber trap. 1064nm laser light from an Azurlight fiber laser source is split into two parts at a PBS. Both parts are sent through an AOM and the 1st diffraction orders are coupled into SM fibers. As the diffraction efficiency of the AOM is dependent on the polarization of the incoming beam a $\frac{\lambda}{2}$ plate is used at AOM 1 to adjust the polarization of the downward propagating beam to horizontal. FG is a dual channel function generator that provides the drive frequency for both AOMs.

light of a 10W Azurlight fiber laser, with central wavelenght $\lambda = 1064$nm, is split into two paths at a PBS. Due to their orientations in the transfer chamber the beams will be referred to as the downward propagating beam (DOWN) and upward propagating beam (UP). Each beam runs through an acousto-optical modulator (AOM) that is supplied with a 80MHz RF signal

at 1W drive power. The signal is generated by a Moglabs XRF421 frequency generator. To improve the diffraction efficiency of AOM1, a $\frac{\lambda}{2}$ plate is used to rotate the polarization to horizontal. The 0th diffraction order is sent into beamdumps, while the 1st order of both beams is sent through telescopes to maximize coupling efficiency into SMs 1 and 2. In this fashion coupling efficiencies of close to 90% were achieved on both ports.

Optical conveyor belt

Fig.13 shows the setup to form the optical conveyor belt within the hollow-core fiber, as well as the alignment and mode-matching optics. A HC-1060 NKT hollow-core fiber is mounted between the vacuum chambers VC1, the smaller loading chamber, and VC2, the science chamber, which also contains the tweezer discussed in section . Inside VC2 the fiber is affixed to a Mechonics MX25 3D piezo positioner stage, to enable alignment between hollow-core fiber and tweezer. The v-groove to mount the fiber with a ferrule and the stage can be seen in Fig.14.

To compensate polarization rotations induced by the fibers, pairs of $\frac{\lambda}{4}$ and $\frac{\lambda}{2}$ plates are placed after SM1 and SM2. The beam originating from SM2 (UP) is expanded in a telescope to allow better coupling into the hollow-core fiber. The mismatch in mode field diameters of HC-1060 ($\approx 6.7\mu m$) and HI-1060 ($\approx 5.9\mu m$), as well as the different coupling lenses made this necessary. A pair of f=40mm and f=60mm focal lenses were chosen to achieve a magnification of M=1.5, expanding the beam to the required diameter.

Following this a PBS is set to control the polarization matching of the standing wave, which can be adjusted with a $\frac{\lambda}{2}$ plate before the coupling lens. The beam is focused down into the fiber through an aspheric lens with a focal length of 18,6mm (Thorlabs TM280-C) mounted on a translation stage. Using these optics it was possible to achieve coupling efficiencies of the upward

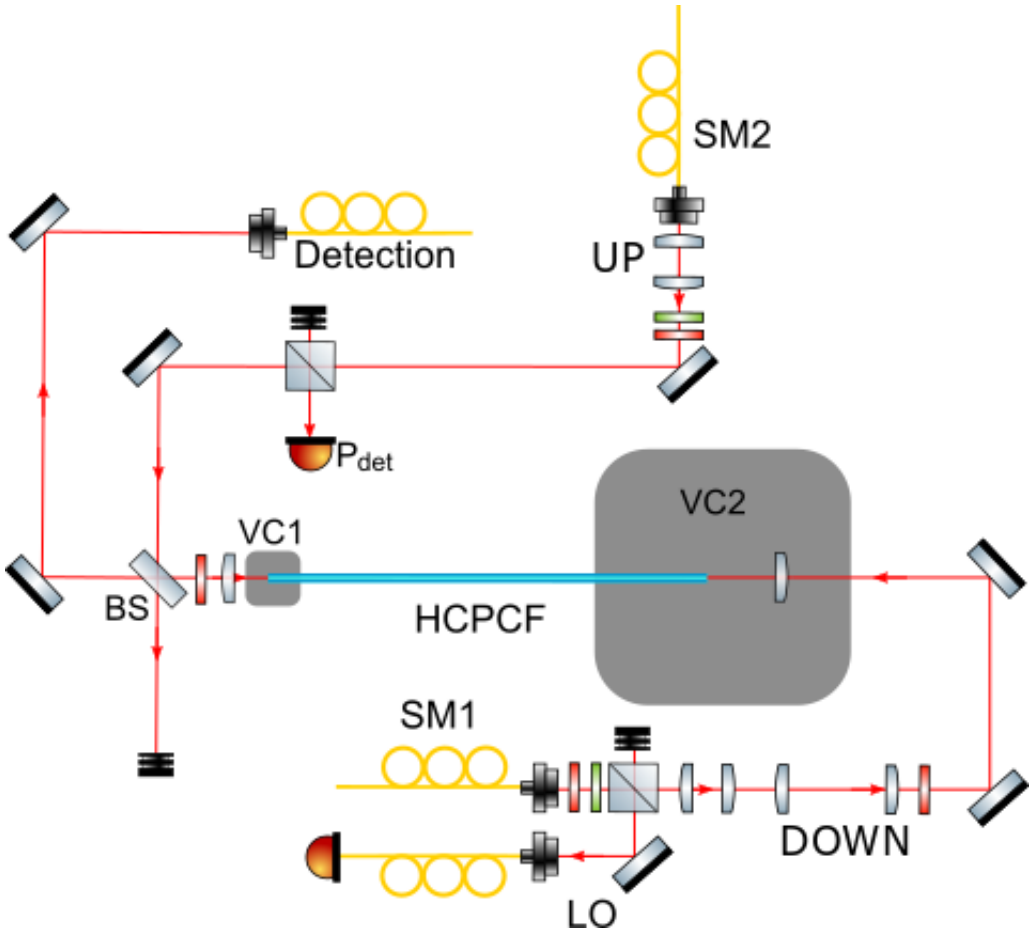

Figure 13: Optical trap section of the conveyor belt setup. The light guided from the beam preparation through optical fibers SM1 and SM2 is coupled into the hollow-core fiber. The upward propagating beam (UP) is expanded in a telescope to increase the coupling efficiency into the hollow-core fiber through the coupling lens in front of VC1. The downward propagating beam (DOWN) is coupled into the hollow-core fiber by utilizing two 1:1 telescopes in addition to a coupling lens in VC2 to achieve a variable focal length. A 90:10 beamsplitter (BS) is used to transmit 10% of the beam exiting the hollow-core fiber (DOWN) for position detection.

propagating beam (η_{up}) into the hollow-core fiber of up to 80%.

The downward propagating beam enters the conveyor belt setup via SM1. After the compensating wave plates a PBS is placed in the beam path, which serves to split the local oscillator (LO) signal from the downward propagating

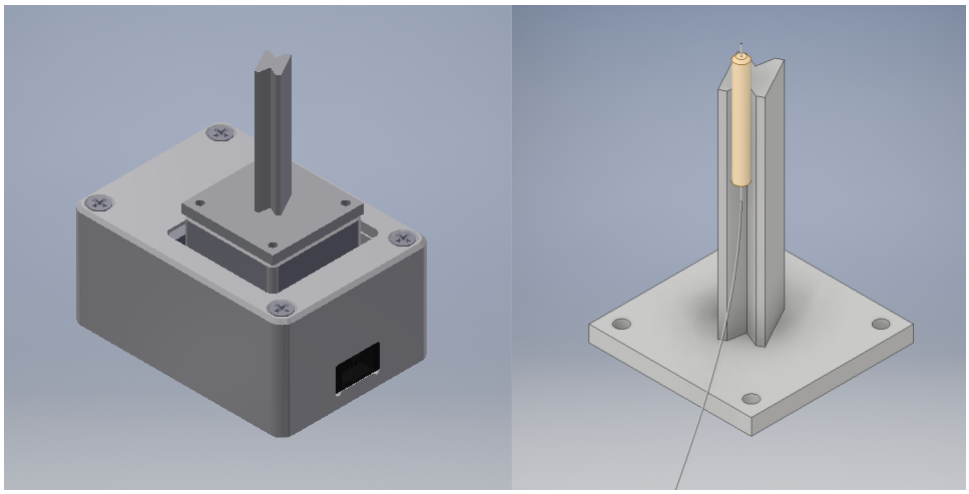

Figure 14: 3D piezo positioner stage used in this experiment. Mounted to the top of the stage is a double sided v-groove for mounting fibers in ferrules vertically, as can be seen on the right. The movement range of the stage is 2mm, with a minimal step size of 6nm.

beam. The LO, together with light of the downward propagating beam leaving the hollow-core fiber through the beamsplitter, is used for axial motion detection. This is accomplished by sending both LO and detection signal to a split photo diode and evaluating the difference signal.

Following this, a pair of 1:1 telescopes is used to control beam size and divergence and allow improved coupling into the hollow-core fiber inside of VC2. To control the standing wave polarization a $\frac{\lambda}{2}$ plate is placed between the telescope and the coupling lens. The downward propagating beam is coupled into the hollow-core fiber using a 11mm focal length aspheric lens (Thorlabs A397), that is mounted above the tip of the fiber. With this configuration high coupling efficiencies into the hollow-core fiber, up to 87%, were achieved over large distances, even with an immobile coupling lens. For operation of the conveyor belt values around 70% were sufficient.

Vacuum Setup

For the requirements of the experiment the vacuum setup was implemented in such a way, that independent pumping of either chamber was possible. Fig.15 shows the two vacuum chambers and their respective valves, gauges and particle source. Note that this is a test setup that is not capable of reaching UHV.

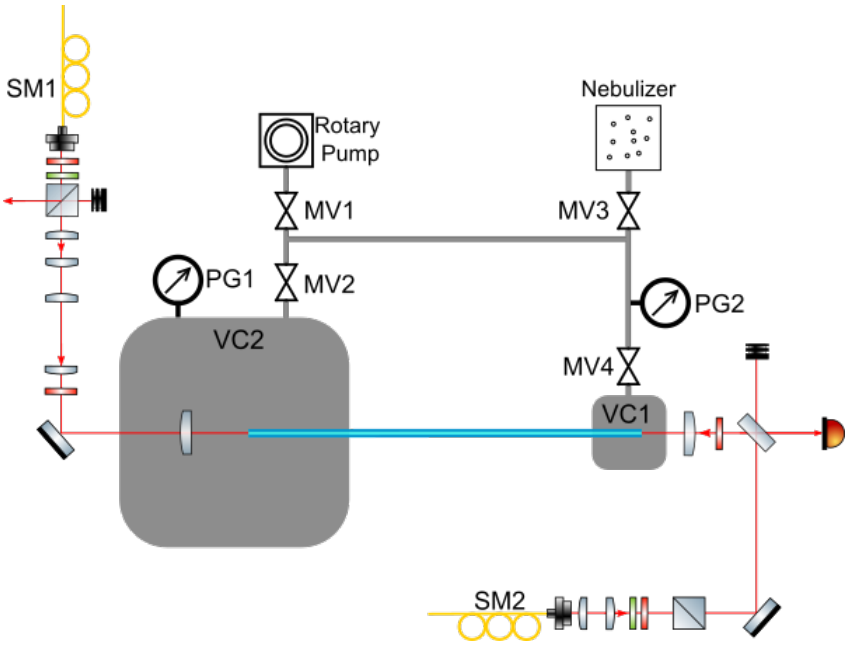

Figure 15: Vacuum configuration for particle transfer. Two vacuum chambers are connected to a single vacuum pump. The connection can be controlled by a series of membrane valves, (MV1-4) allowing independent pumping by using MV1 and MV2 for VC2 or MV1 and MV4 for VC1. Particles from the nebulizer particle source can also be loaded into either chamber in similar fashion (opening/closing MV3 instead of MV1). Each vacuum chamber is fitted with a vacuum gauge (PG1 and PG2).

The two chambers used in this experiment were a smaller loading chamber (VC1) where particles are loaded into the hollow-core fiber and a larger science chamber, in which the tweezer trap, piezo-positioner and one end of the hollow-core fiber were placed.

Both vacuum chambers were connected to the same roughing pump, with a

series of valves that allow for pumping and loading both chamber separately. By operating valves MV1 and MV2 VC2 can be pumped and loaded while keeping pressure in VC1 stable. Similarly VC1 can be operated via valves MV1 and MV4.
The method for mounting the hollow-core fiber in VC1 is covered in the thesis of David Grass[50].

The hollow-core fiber was inserted into the test chamber through a CF16 flange with a drilled through-hole, that was sealed with UV curing glue. Inside VC2 it was mounted on a v-groove and 3D stage as mentioned above.

Summary

This chapter introduced the different sections of the experimental setup to demonstrate and test handovers between an optical tweezer and an optical conveyor belt.

RESULTS

This chapter covers the characterization of the optical tweezer, the procedure for aligning the optical conveyor belt with the tweezer trap and the process of transferring particles between the two. The results are compared with predictions from chapter .

The hollow-core fiber used in the transfer is susceptible to contamination if the loading is performed incorrectly. For this reason a proper procedure, that prevents damage to the fiber, must be adhered to. All particles used in the experiment had a diameter of $d_p = 245 \pm 3nm$.

Wet Loading the Tweezer

After proper alignment of the optical tweezer, particles from a nebulizer source can be trapped directly in the science chamber. In our setup loading works properly in a pressure range from 300mBar to room pressure.

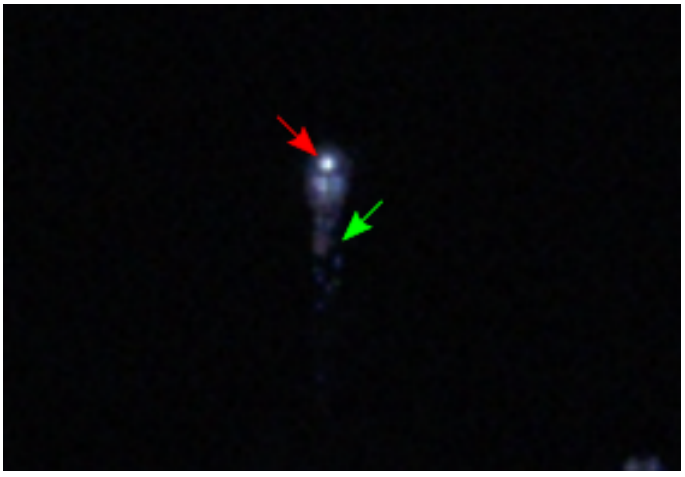

Figure 16: 245nm diameter particle (red arrow) trapped in the tweezer trap, close to the hollow-core fiber (green arrow). Distance between particle and fibertip is around $90\mu m$.

Starting with an aligned tweezer the trapping procedure is as follows: Firstly, VC1 is flooded with clean air, to prevent particles from travelling into the hollow-core fiber due to gas drag, which may cause clogging of the fiber.

Secondly, VC2 is evacuated and subsequently flooded with particles from the nebulizer source in a controlled fashion, typically by setting MV2 such that the pressure rises by approximately 10mbar/s. The particle-water solution (Microparticles GMBH:SiO2-R-0.25) used for loading is diluted in isopropanol to achieve a mass-solvent concentration of 10^{-4}. Capturing a particle in the tweezer can take 5-10 minutes, with increasing times observed when the solution isn't freshly prepared.

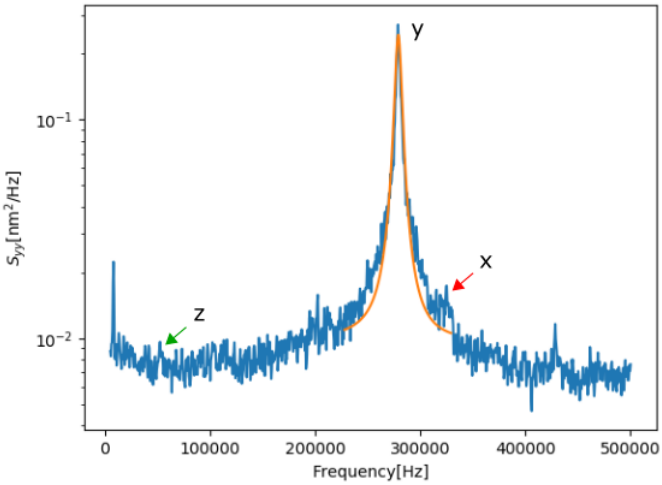

Figure 17: Power spectral density (PSD) of the tweezer detection signal. The signal exhibits 3 peaks, that correspond to different motional directions of the particle in the tweezer trap. Due to the configuration of the detection the motion along the fiber axis is most pronounced, while the orthogonal directions are suppressed. Axially (green arrow), where the confinement is weakest, the frequency is lowest. The frequency of the 2 radial directions are comparable, with the motion along the fiber axis exhibiting a slightly lower frequency of $f_y = 278 \pm 4$kHz.

Once a particle is trapped the chamber is evacuated down to 0.5 mBar for several minutes, before increasing the pressure to 5 mBar. To our current knowledge ([54] [55]) this procedure evaporates any isopropanol or water adhering to the particle and ensures that the trapped particle is indeed a SiO_2 nanosphere. The PSD of the particle motion, at 1.2W tweezer power measured

in front of the vacuum chamber, can be seen in Fig.17.

To partially compensate for radiaton pressure effects along the tweezer axis, the beam is reflected back through the low NA collection lens, as seen in Fig.10. By matching the polarization of the reflected beam we generated a standing wave in the tweezer. The alignment of the back reflected beam can be optimized by maximizing the axial particle frequency. Due to the large discrepancy in numerical apertures of trapping and collection lens the standing wave is mismatched.

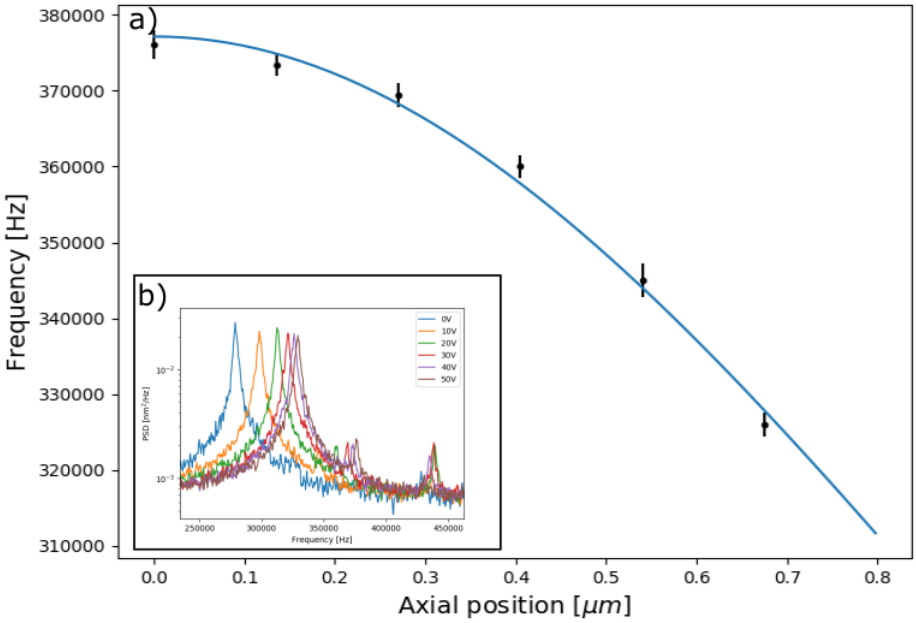

Figure 18: Radial x frequencies of a trapped particle for different positions along the tweezer axis. For each position along the beam we determine the power spectral densities of the transversal particle motion. As the square of the beam waist is indirectly proportional to the frequency (see eq.21), we can use this to characterize the Gaussian mode shape. In a) a plot of frequency over displacement (dots) is fitted with the theoretical curve (line) to extract the minimal waist of the tweezer, approximately 768 $\pm$ 9nm. The inset b) shows the power spectral density for the different positions along the tweezer axis.

The mirror in the reflection arm can be moved by changing the voltage

applied to the piezo-transducer at the mirror. The change in optical path length moves the standing wave maxima along the tweezer axis, which in turn moves a particle confined to one such maximum. In this way the motion of the particle is evaluated at at several positions along the beam axis. By calculating the power spectral densities of particle motion and fitting the frequencies (see eq.21) obtained from these as a function of the displacement the minimal waist of the trap can be determined. In this fashion the tweezer waist was determined to be approximately 768 ± 9 nm, as shown in Fig.18. This is larger than the beam waist predicted in the paraxial approximation by close to a factor of 2.

Alignment

The coordinate system we will use for discussion of the alignment can be seen in Fig.19.

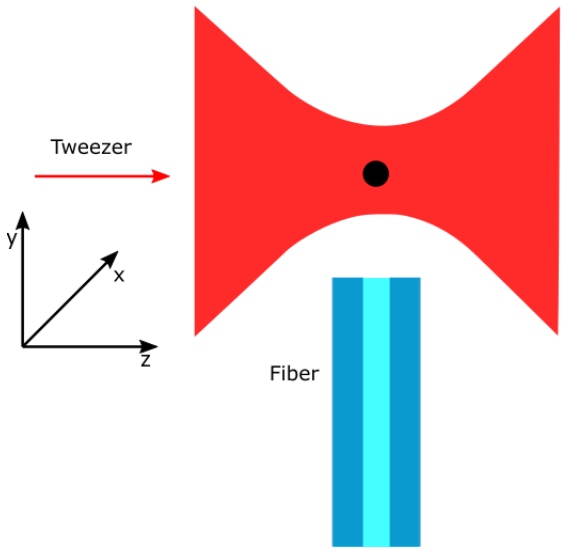

Figure 19: Representation of the relative position of tweezer and fiber (not to scale). The coordinates given as z (along tweezer), x (Orthogonal to tweezer axis and fiber) and y (along fiber).

To allow for handovers between the optical conveyor belt and the tweezer it is necessary to position the hollow-core fiber correctly relative to the tweezer

trap. This positioning is performed in 3 steps with increasing accuracy.

Rough positioning:

Initially the relative positions of hollow-core fiber and tweezer are unknown. The 2mm range of motion of the stage used in this thesis allowed for positioning the hollow-core fiber in tweezer proximity, using footage from a CCD camera. By observing the scattered light when moving the fiber through the beam laterally and axially a position close to the waist was found.

Finer positioning:

Here we used a particle trapped in the tweezer (see Fig.19). By scanning the fiber across the tweezer at incremental distances along the y-axis one starts to observe a reduction in trap frequency, caused by the fiber influencing the trap. The fiber should not be moved too far into the beam, to prevent the trapped particle from being lost. A 2% reduction in particle frequency is sufficient for positioning. By moving the fiber once completely through the fiber one can center the fiber with respect to the tweezer with good accuracy.

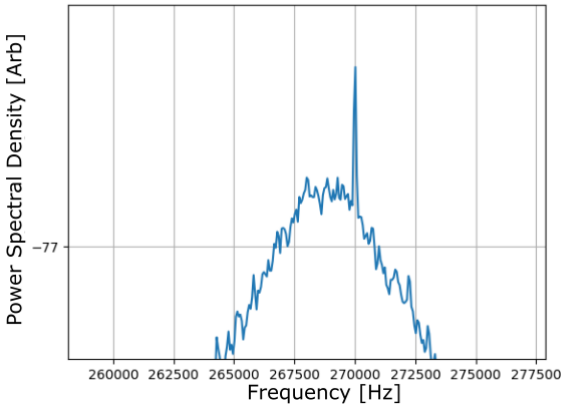

Figure 20: Example spectrum exhibiting the particle response to the radiation pressure drive at 270kHz frequency (narrow peak). The broad peak corresponds to the harmonic motion of the particle.

High precision positioning:

Final positioning used the radiation pressure force of a modulated beam sent through the hollow-core fiber to displace the particle. To this end, the upwards propagating beam is coupled into the hollow-core fiber with sufficient power to ensure around 600mW in transmission. By modulating the light the radiation pressure force leads to a displacement that is visible in the power spectral density. The modulation is performed using the Moglabs controlling AOM2, with an external signal generator used to alter the modulation frequency as desired. Setting the frequency of modulation to be resonant with the oscillation along the fiber beam propagation axis increases the amplitude of the signal, facilitating the positioning. The response to the modulation can be seen in Fig.20.

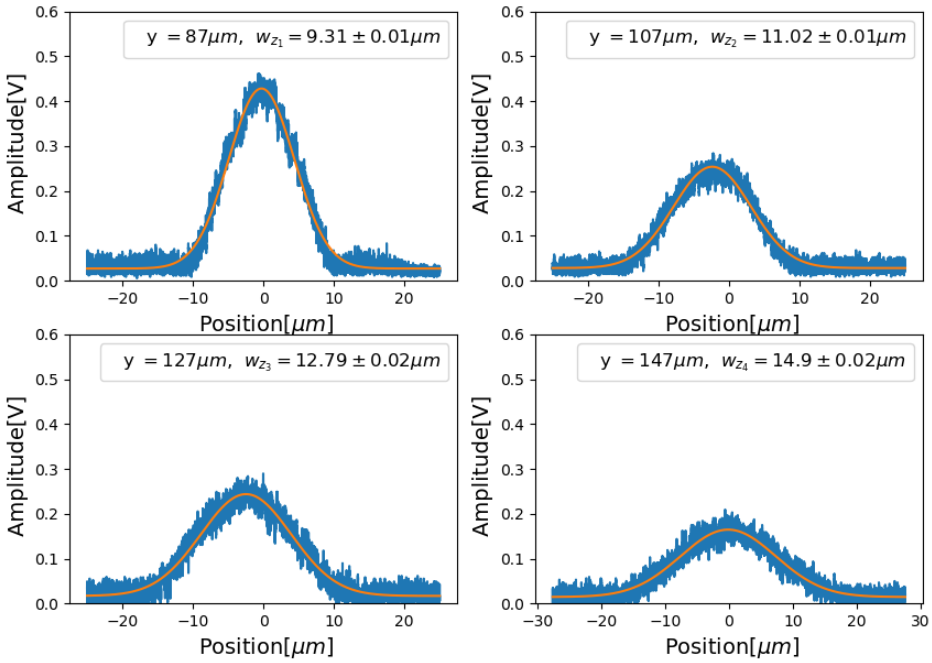

Figure 21: Position dependent particle amplitude for different y-positions of the hollow-core fiber. The position dependent response of the particle driven by radiation pressure is measured by scanning the fiber position. By fitting the data with a Gaussian shape the widths of the Gaussian at different y-positions can be extracted and used to characterize the fiber beam.

Once the frequency is set the driven particle signal is amplified using a lock

in amplifier (Liquid Intruments Moku:Labs). The closer the particle is to the center of the hollow-core fiber beam, the stronger the particle is driven by the radiation pressure force. We use thee amplitude of the signal to determine the optimal position of the hollow-core fiber.

This method allows positioning of the fiber with an accuracy of around 1 μm, as smaller steps do not result in a measurable change in signal amplitude. Scanning multiple times at different distances from the tweezer allows the beam divergence to be characterized. Fig.21 shows scans along the z-direction for increments of $20\mu m$ along y. Fig.22 shows similar measurements made along the x-axis, at the same y-positions.

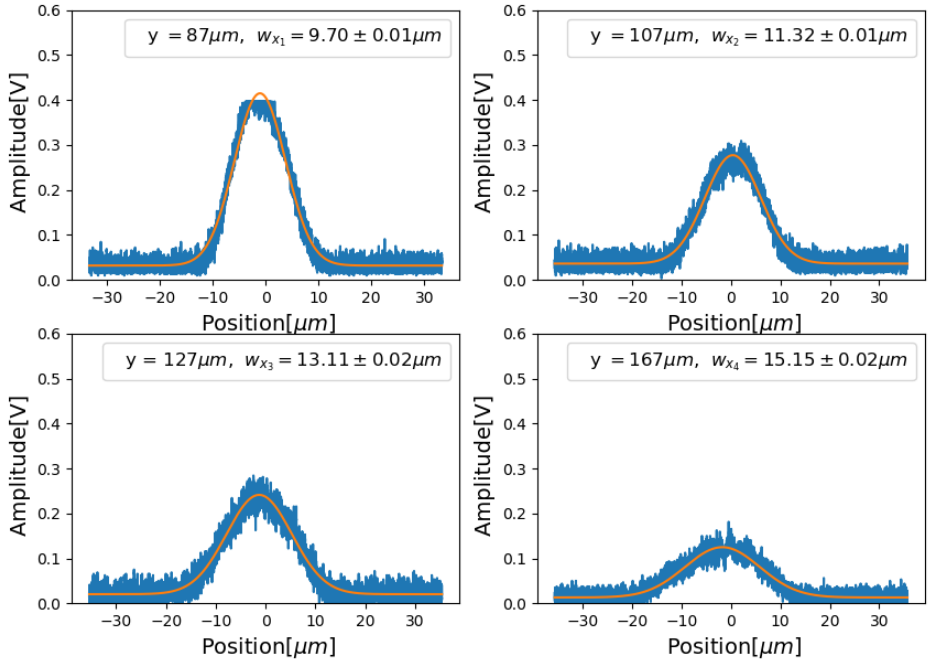

Figure 22: Position dependent signal amplitude for scans across the tweezer, the x-direction according to Fig.19). The Gaussian shapes of the position dependent amplitude are again fitted with a Gaussian lineshape, to extract the beam waist from the data. This gives another set of points for determining the parameters of the hollow-core fiber beam.

The position dependent beam waist is plotted in Fig.23. By fitting a Gaussian beam profile to the data we obtain a divergence angle of 97.4 ± 3.1mrad corresponding to a minimal waist of $w_{min,z} = 3.48 \pm 0.11\mu$m at the fiber exit

along x and $w_{min,x} = 3.56 \pm 0.10\mu$m along z, both of which are consistent with the manufacturer specifications of $w_{mf} = 3.35 \pm 0.5\mu$m [56]. Note, that this also allows to determine the distance between the particle and the hollow-core fiber tip during the measurements. This defined the 0-position, as used in Figs.21 and 22. This distance was found to be $87 \pm 4\mu m$.

As we can see, there is a mismatch in the waist between the two orthogonal scanning axes. This can be explained if the measurements are not performed in a plane that is completely orthogonal to the beam axis of the hollow-core fiber. The data is consistent with an angle relative to the orthogonal plane of $7.50 \pm 1.6°$. In other words, the beam axis is tilted by 7.50 degrees with respect to the x-z plane scanned by the translation stage.

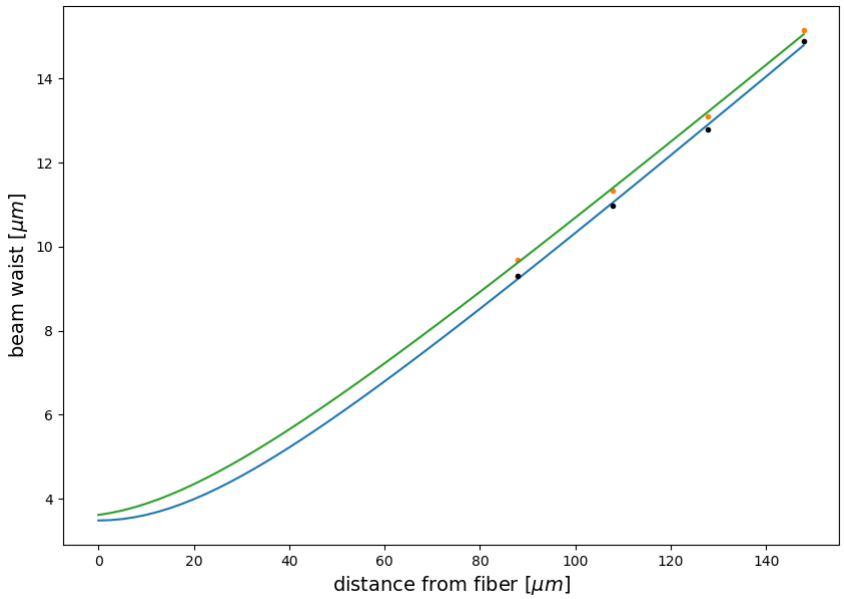

Figure 23: Plot of the waist values extracted from Figs.21 and 22 fitted with Gaussian beam waist. The scans performed along the tweezer axis (black) and across the tweezer (orange), allowed the extraction of minimal waists of $w_{min,z} = 3.48 \pm 0.11\mu$m (black) and $w_{min,x} = 3.56 \pm 0.10\mu$m (orange), at the fiber tip. The slight mismatch in the results for the scanning directions can be attributed to a slight deviation from the right angle between scanning plane and fiber axis.

An issue we encountered with this high precision alignment is the sensitivity

of the lock-in signal to fluctuations in laser power, that are caused by polarization and thermal drifts. Fluctuations in the trapping beam power lead to shifts in particle frequency, that influence the signal amplitude. Power changes of the fiber beam affect the scattering force and thereby the amplitdue of the lock-in signal. In addition to this position drifts of the hollow-core fiber impair the signal. Such drifts have been independently observed on a position sensitive detector.

The drifts are so small that the alignment between hollow-core fiber and tweezer remains sufficient for transfer of particles. Once positioned, the configuration typically remains aligned for several days.

The final preparatory step for particle transport is to couple the downward propagating beam into the hollow-core fiber and to maximize the transmission by controlling the polarization. The conveyor belt is ready for transport once this step is complete.

Particle transfer

In this section we will describe process of transferring particles between tweezer and conveyor belt. Table.II lists the experimental parameters of the transfer. The optical powers were measured in front of the vacuum chambers.

$P_{tweezer}$	P_{down}	P_{up}	η_{up}	η_{down}	$d_{particle}$	Pressure
126±5mW	2.00 ±0.05W	1.30±0.05W	75±2%	77±2%	245±3nm	5mBar

Table II: Experimental parameters used throughout this section. The parameters are laser power of tweezer ($P_{tweezer}$), downward and upward propagating beams (P_{up} & P_{down}) as well as coupling efficiencies into the hollow core fiber of these beams (η_{up} & η_{down}) as well as the particle diameter $d = 2a$ and Pressure.

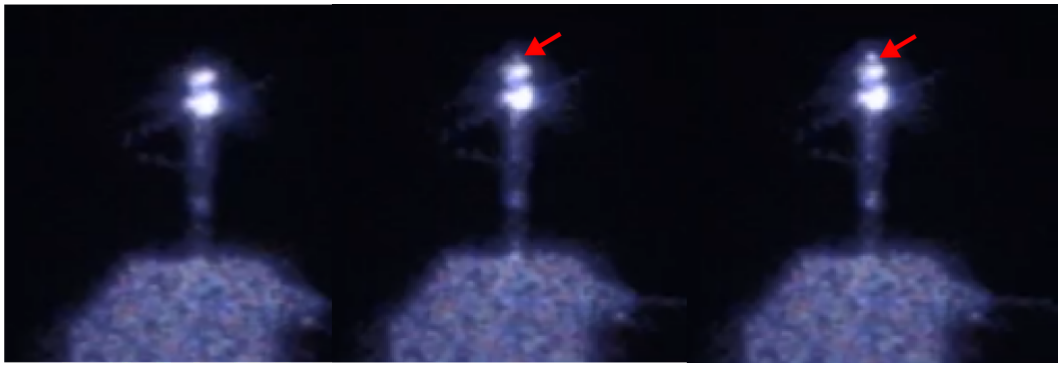

Figure 24: Image of the trapping configuration without particle (left), a particle trapped in the conveyor belt outside the fiber (middle) and the same particle trapped in the optical tweezer trap (right).

The cross-section of the standing wave trap, given by hollow-core fiber beam, is much larger than that of the optical tweezer. For this reason transferring particles into the conveyor belt and further into the fiber is possible without much difficulty. A particle is transferred by moving the optical conveyor belt towards the fiber. To do this, a negative relative detuning of the

frequency of the upward propagating beam is set. In this case the detuning, $\Delta = -1\text{kHz}$, results in a conveyor belt velocity of approximately 0.532mm/s. By reducing the laser power of the tweezer trap to below 120 mW the particle is eventually pulled out of the trap. The corresponding particle trajectory can be seen in Fig.25.

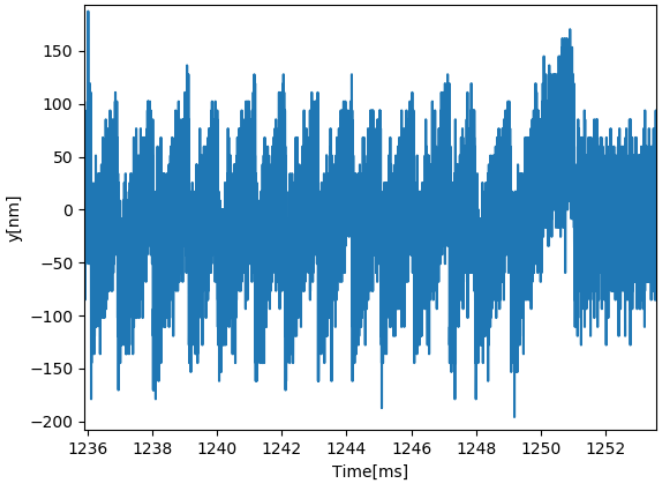

Figure 25: Timetrace of the particle motion during tweezer to fiber handover. A detuning of 1kHz was used, which is reflected in the periodicity of the jumps observable in the signal with an approximate conveyor belt velocity of 0.532mm/s. Here we set a threshold power of 120mW in the tweezer, allowing the particle to be pulled out of the tweezer trap by the conveyor belt.

It shows the detection signal of the tweezer during the transfer. In this timetrace the particle signal shows periodic jumps. These occur at 1ms intervals, reflecting the 1kHz detuning used for the transfer. At $t = 12.5\text{ms}$, the signal stops, indicating the removal of the particle from the tweezer. For verification of the successful transfer the image of a CCD camera, such as in Fig.24, can be used showing the particle in the hollow-core fiber.

The loading procedure from conveyor belt to tweezer trap is more challenging, as it requires more accurate positioning due to the smaller cross section of

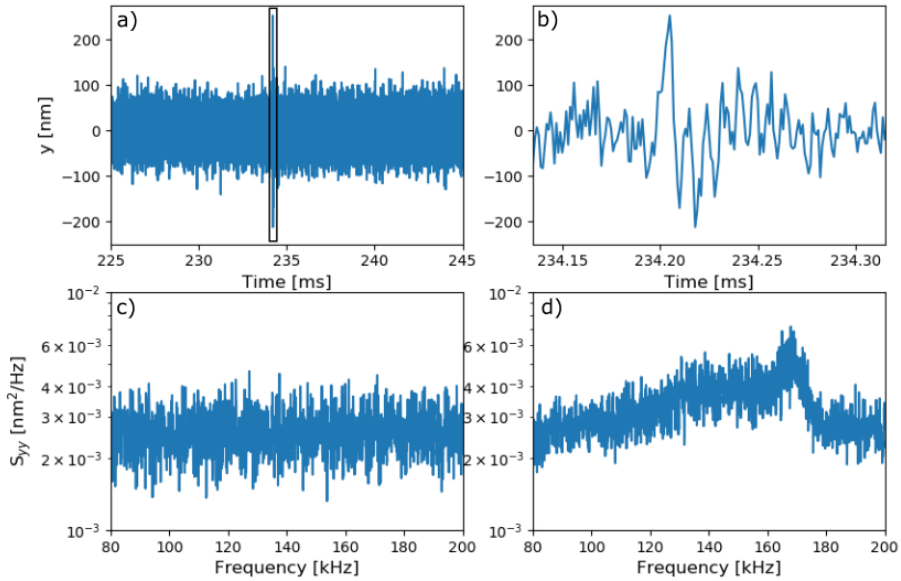

Figure 26: Timetrace of the tweezer split detection signal during a handover from conveyor belt to tweezer at 10Hz detuning. Top row a) shows the initial spike in the detection as the particle enters the tweezer trap. b) Zoom into the signal shows a ringdown after capture. c) PSD of tweezer readout before the transfer, showing no particle is in the tweezer. d) PSD of detected signal after the transfer, exhibiting the motional peaks that indicate a particle. The width of the signal is caused by the movement of the standing wave across the tweezer trap, resulting in different motional frequencies depending on standing wave position.

the tweezer trap. Successful transfers took place at 125mW of laser power in the tweezer trap, as well as powers of $P_{down} = 2$W and $P_{up} = 1$W inside VC2. To prevent radiation pressure forces from destabilizing the particle during transfer the reflection arm of the tweezer should be open, to compensate the scattering force acting on the particle. The reflected beam is set to have orthogonal polarization to the trap beam, such that no standing wave is created in the tweezer.

To transfer the particle into the tweezer it is moved out of the fiber at a detuning of 10Hz. Fig.26 shows the particle position readout in the tweezer. We determined the moment of transfer by evaluating the power spectral densities

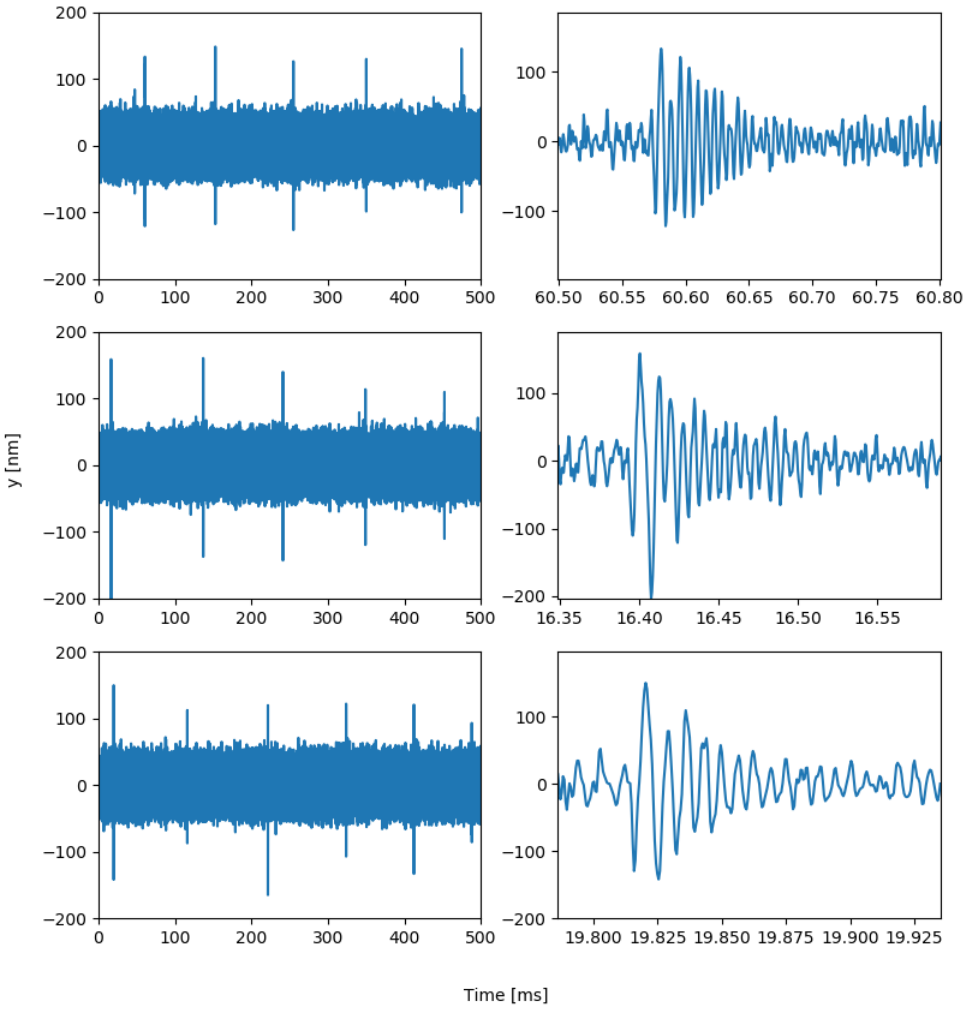

Figure 27: Timetraces of particle motion with conveyor belt detuning at 10Hz. On the left complete 500ms timetraces after handover can be seen. As the particle is still co trapped in the conveyor belt it is pulled along the moving intensity maxima. Large displacements occur when the particle "falls" back into the tweezer. At the maximal displacement the gradient force pulling the particle back is approximately 10 pN. These peaks occur at 10Hz frequency on average, conforming to the theoretical prediction. On the right zoomed sections of the initial ringdown can be seen.

before and after the initial spike in displacement. The displacement observed is followed by a ringdown of the the particle. Multiple similar handovers at 10Hz can be seen in Fig.27. The periodic spikes in displacement are caused by the particle being pulled along with the conveyor belt, before falling back

into the tweezer trap. The maximum displacement of the particle from the zero point, approximately 150nm, indicates that a force of 10pN is required to remove a nanoparticle from the conveyor belt. This is consistent with the maximal force the standing wave trap can exert on a particle. The time between these spikes in displacement is approximately 100ms, conforming to what we would expect at 10Hz detuning.

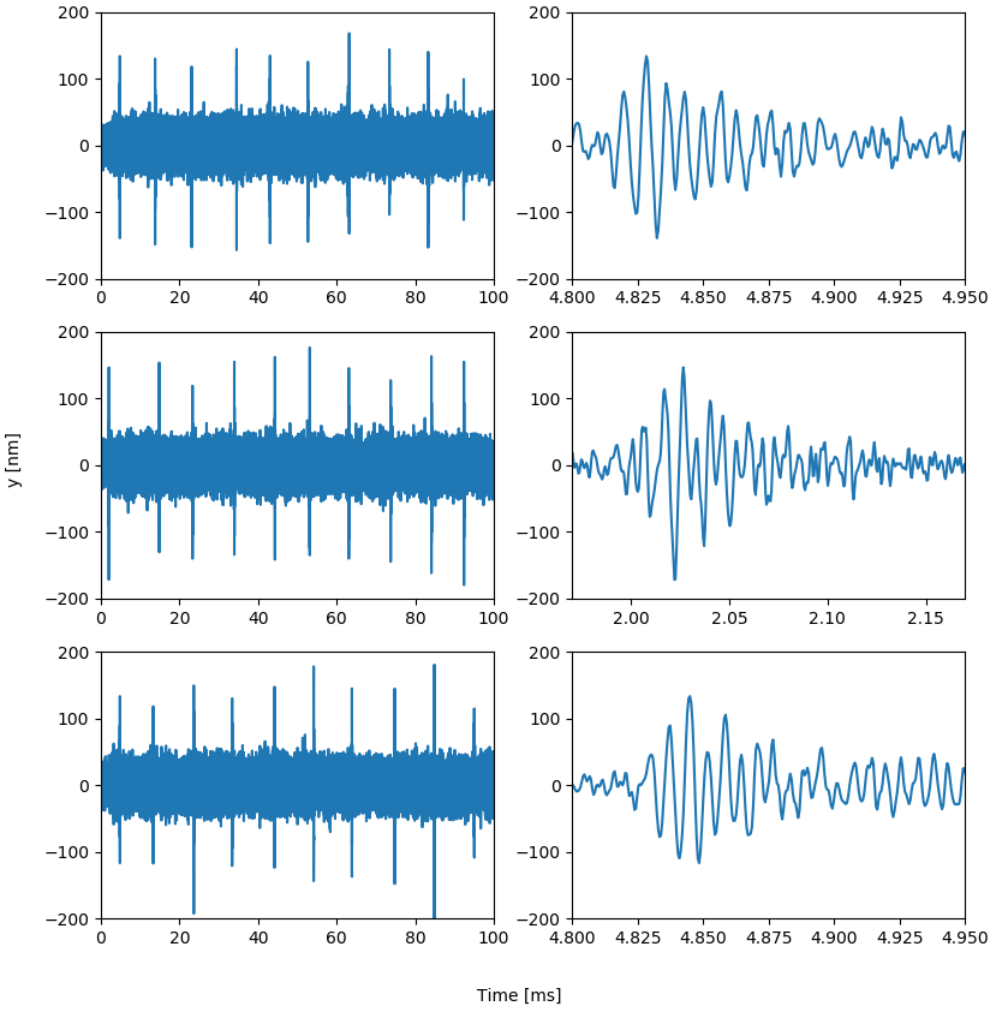

Figure 28: Timetraces of particle motion with conveyor belt detuning at 100Hz. Similar to detunings of 10Hz particles are pulled along with the conveyor belt, before "falling" back into the tweezer trap with a ringdown. The time interval between these spikes in displacement is on average 10ms, conforming to our expectation from the detuning.

Similar behaviour was observed for loading attempts made at a detuning of Δ =100Hz. The time between the displacement spikes and subsequent ringdown, as seen in Fig.28, is 10ms on average, which is expected for the detuning set. The maximum displacement before the particle is pulled back into the tweezer is between 100 and 200 nm. At this position the gradient force on the particle is again approximately 10pN.

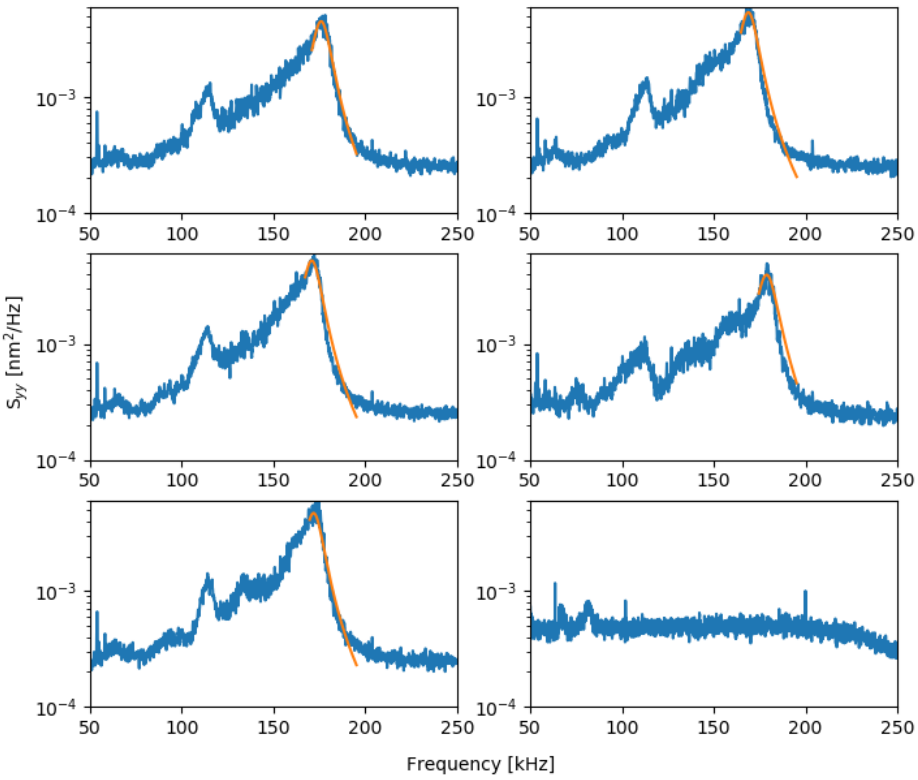

Figure 29: Power spectral densities calculated from 5 handover timetraces. The traces were bandpass filtered from 40-300 kHz. Handovers were performed at a detuning of 10Hz. By applying a narrow bandpass of 50kHz bandwidth around the maximal observed frequency the response curve was determined. The maximal frequencies fall close to the theoretically expected value calculated from the experimental parameters of $\approx$ 170kHz. The PSD on the bottom right shows the signal before a particle is transferred into the tweezer.

The power spectral densities of the particle motion in the first 500ms after handover can be seen in Fig.29. The data was filtered using a bandpass from 40-300kHz. The motional peaks appear washed out, as the position of the standing wave maxima affects the particle frequency. The maximal frequency is observed during full overlap of standing wave and tweezer trap. Using eq.36 with the data from characterization of the tweezer and standing wave, this maximal frequency can be accurately predicted. The theoretical particle frequency calculated is approximately 170kHz, which falls within the range of the observed frequencies and their errors.

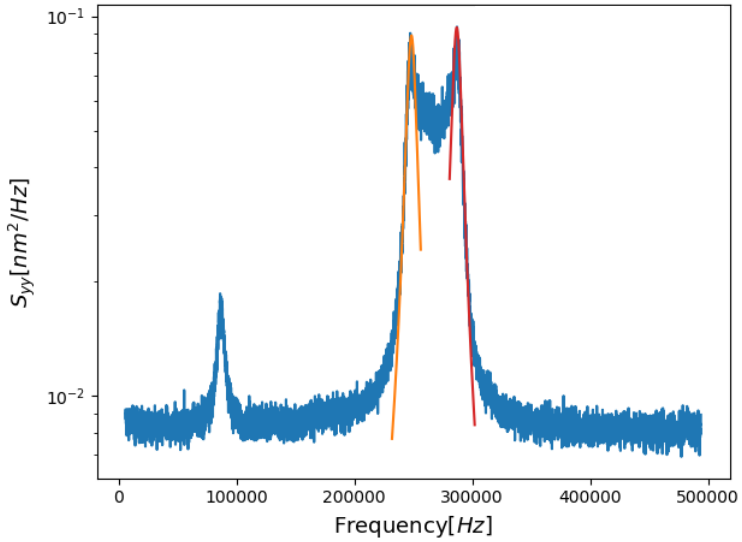

Figure 30: PSD of the detection signal for combined trap (conveyor belt and tweezer) without detuning. The the influence of the standing wave position fluctuating is clearly visible on the motional peak corresponding to the y-direction, sometimes adding to, sometimes compensating the tweezer. The frequency ranges between f_{min} = 248±5 kHz and f_{min} = 288±6 kHz.

Once the particle is transferred the power in the tweezer can be increased and the detuning deactivated. The resulting power spectral density can be seen in Fig.30. Two peaks can be seen for the motion along the conveyor

belt axis. This is due to the fluctuations of optical path length, that cause the standing wave maxima to alternatively overlap with the tweezer, or to compensate it. The maximal frequency, approximately 288 ± 6kHz, is close to the theoretical prediction if the 269kHz frequency observed in the tweezer trap is taken into account. By doing so the predicted frequency, following $f_{y,comb} = \sqrt{f_{yreal,tweezer} + f_{y,cw}}$, turns out to be 294kHz.

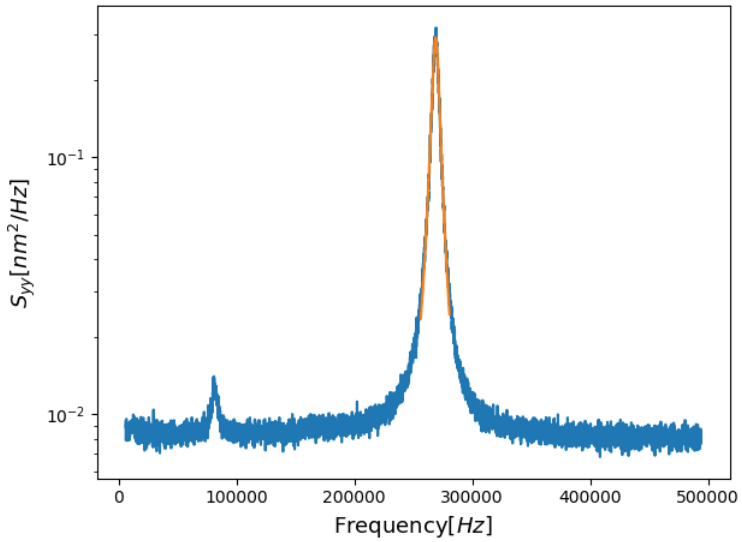

Figure 31: PSD of the detection signal after the conveyor belt through the hollow-core fiber is deactivated. The motional peak corresponding to the y-direction is clearly visible at $f_y = 269 \pm 3$ kHz, while the x-motional peak is not visible, similar to the signal before the particle was transported into the conveyor belt.

Fig.31 shows the PSD once the power in the standing wave is reduced below 100mW. The effects the standing wave has on the particle motion are no longer visible. While the spectral peak of the motion along the x-axis is not visible, the motional frequency along the y-axis is similar to the one observed previously.

Summary

The data presented in this chapter demonstrated the achievement of particle transfer between an optical conveyor belt and an optical tweezer at mBar pressures. By using modulated radiation pressure force the two traps were repeatably and reliably aligned, with sufficient precision to allow transfers with good efficiencies. In addition, the positioning allowed the characterization of the beam used to generate the standing wave trap, as well as extract the distance between the fiber tip and the tweezer trap.

The optimal transfer procedure consisted of using low optical powers in the tweezer trap and a compensation mechanism for the scattering force in the form of a reflected beam. A transfer efficiency close to 1 could be achieved by using a detuning of 10Hz. We estimated the force necessary to dislodge a particle from the conveyor belt by the maximal displacement observed during ringdown events. Additionally to this, the particle frequencies we measured fell into the ranges predicted by the theory, certifying its usefulness for describing the combined trapping potential.

CONCLUSIONS AND OUTLOOK

In this thesis we concluded that ultrahigh vacuum is a precondition to observing the effects of blackbody radiation on quantum states. We argued that the scattering, absorbtion and emission of blackbody radiation are of special interest, as these will fundamentally limit the lifetime of any quantum state that can be generated in an experiment. To quantify the magnitude of the interaction we proposed an experiment to measure how the diffusion rate of a ground state wavefunction is influenced by blackbody radiation. We calculated the parameters necessary for experimental observation, finding that pressures below 10^{-11} mBar and temperatures above 1400K are required. To achieve the necessary pressures we proposed a loading mechanism to load into XUHV. We successfully implemented the method proposed in this thesis, loading via a hollow-core photonic crystal fiber and demonstrated alignment and transfer of a particle between hollow-core fiber and optical tweezer in low vacuum conditions.

Looking forward, many experimental challenges still need to be addressed. One foreseeable issue is loss of particles from the optical conveyor belt at lower pressures, such as occurred in optical traps below 1 mBar [31]. Another issue is the current reliance of successful loading on gas damping. Improvements to remove this reliance are necessary. This can be accomplished by setting a trigger to switch the optical potential, or timed switching of the trap, such as performed in [46]. Doing so will allow nanoparticles to enter the trap without experiencing the full potential, removing the reliance on gas damping. This is a good way to allow loading directly into UHV.

In addition to an improved loading scheme, a test of blackbody radiation induced diffusion of the wavepacket will require ground state cooling, such as [39] or [57], and position readout sensitivity at the quantum limit. The requirement particle recapture can be addressed by using an AOD, as seen in [21], to generate a mobile optical tweezer.

All these prerequisites are on the edge of what is currently possible and will require further development to be usable in experiments that test quantum

physics. The knowledge gained from the planned experiment could lead to studies with different particle geometries or materials. From there particles could be designed to minimize the influence of blackbody radiation on quantum states, or even turn them into a beneficial effect.

REFERENCES

[1] Y. Y. Fein, P. Geyer, P. Zwick, F. Kiałka, S. Pedalino, M. Mayor, S. Gerlich, and M. Arndt, "Quantum superposition of molecules beyond 25 kda," Nature Physics **15**, 1242–1245 (2019).

[2] O. Romero-Isart, A. C. Pflanzer, F. Blaser, R. Kaltenbaek, N. Kiesel, M. Aspelmeyer, and J. I. Cirac, "Large quantum superpositions and interference of massive nanometer-sized objects," Physical review letters **107**, 020405 (2011).

[3] H. Pino, J. Prat-Camps, K. Sinha, B. P. Venkatesh, and O. Romero-Isart, "On-chip quantum interference of a superconducting microsphere," Quantum Science and Technology **3**, 025001 (2018).

[4] U. Delić, M. Reisenbauer, K. Dare, D. Grass, V. Vuletić, N. Kiesel, and M. Aspelmeyer, "Cooling of a levitated nanoparticle to the motional quantum ground state," Science **367**, 892–895 (2020).

[5] F. Tebbenjohanns, M. Frimmer, V. Jain, D. Windey, and L. Novotny, "Motional sideband asymmetry of a nanoparticle optically levitated in free space," Physical Review Letters **124**, 013603 (2020).

[6] R. Kaltenbaek, G. Hechenblaikner, N. Kiesel, O. Romero-Isart, K. C. Schwab, U. Johann, and M. Aspelmeyer, "Macroscopic quantum resonators (maqro)," Experimental Astronomy **34**, 123–164 (2012).

[7] K. Hornberger, L. Hackermüller, and M. Arndt, "Influence of molecular temperature on the coherence of fullerenes in a near-field interferometer," Physical Review A **71**, 023601 (2005).

[8] T. P. Weldon, "Rayleigh and mie enhancement of blackbody radiation in nanoscale devices," in *IEEE Southeastcon 2009* (IEEE, 2009) pp. 216–220.

[9] I. Sister, Y. Leviatan, and L. Schächter, "Evaluation of blackbody radiation emitted by arbitrarily shaped bodies using the source model technique," Optics express **25**, A589–A601 (2017).

[10] P. Haslinger, M. Jaffe, V. Xu, O. Schwartz, M. Sonnleitner, M. Ritsch-Marte,

H. Ritsch, and H. Müller, "Attractive force on atoms due to blackbody radiation," Nature Physics **14**, 257–260 (2018).

[11] V. Jain, J. Gieseler, C. Moritz, C. Dellago, R. Quidant, and L. Novotny, "Direct measurement of photon recoil from a levitated nanoparticle," Physical review letters **116**, 243601 (2016).

[12] D. Grass, J. Fesel, S. G. Hofer, N. Kiesel, and M. Aspelmeyer, "Optical trapping and control of nanoparticles inside evacuated hollow core photonic crystal fibers," Applied Physics Letters **108**, 221103 (2016).

[13] M. Planck, *The theory of heat radiation* (Courier Corporation, 2013).

[14] Y. V. Martynenko and L. Ognev, "Thermal radiation of conducting nanoparticles," arXiv preprint physics/0503025 (2005).

[15] J. Cuevas, "Thermal radiation from subwavelength objects and the violation of planck's law," Nature Communications **10**, 3342 (2019).

[16] E. Joos and H. D. Zeh, "The emergence of classical properties through interaction with the environment," Zeitschrift für Physik B Condensed Matter **59**, 223–243 (1985).

[17] O. Romero-Isart, "Quantum superposition of massive objects and collapse models," Physical Review A **84**, 052121 (2011).

[18] G. M. D'Ariano and H. Yuen, "Impossibility of measuring the wave function of a single quantum system," Physical review letters **76**, 2832 (1996).

[19] R. Kaltenbaek, M. Aspelmeyer, P. F. Barker, A. Bassi, J. Bateman, K. Bongs, S. Bose, C. Braxmaier, Č. Brukner, B. Christophe, *et al.*, "Macroscopic quantum resonators (maqro): 2015 update," EPJ Quantum Technology **3**, 5 (2016).

[20] P. Manini, "Non evaporable getter (neg) pumps: a route to uhv-xhv," in *AIP Conference Proceedings*, Vol. 1149 (2009) pp. 1138–1142.

[21] M. Endres, H. Bernien, A. Keesling, H. Levine, E. R. Anschuetz, A. Krajenbrink, C. Senko, V. Vuletic, M. Greiner, and M. D. Lukin, "Atom-by-atom assembly of defect-free one-dimensional cold atom arrays," Science **354**, 1024–1027 (2016).

[22] A. Ashkin, "Acceleration and trapping of particles by radiation pressure," Physical review letters **24**, 156 (1970).

[23] A. Ashkin and J. Dziedzic, "Feedback stabilization of optically levitated particles," Applied Physics Letters **30**, 202–204 (1977).

[24] A. Ashkin and J. Dziedzic, "Optical levitation in high vacuum," Applied Physics Letters **28**, 333–335 (1976).

[25] N. Li, X.-m. Zhu, W.-q. Li, Z.-h. Fu, M.-z. Hu, and H.-z. Hu, "Review of optical tweezers in vacuum," Frontiers of Information Technology & Electronic Engineering **20**, 655–673 (2019).

[26] Y. Harada and T. Asakura, "Radiation forces on a dielectric sphere in the rayleigh scattering regime," Optics communications **124**, 529–541 (1996).

[27] L. Novotny and B. Hecht, *Principles of Nano-Optics*, 2nd ed. (Cambridge University Press, 2012).

[28] S. Beresnev, V. Chernyak, and G. Fomyagin, "Motion of a spherical particle in a rarefied gas. part 2. drag and thermal polarization," Journal of Fluid Mechanics **219**, 405–421 (1990).

[29] D. Schrader, S. Kuhr, W. Alt, M. Müller, V. Gomer, and D. Meschede, "An optical conveyor belt for single neutral atoms," Applied Physics B **73**, 819–824 (2001).

[30] J. Gieseler, B. Deutsch, R. Quidant, and L. Novotny, "Subkelvin parametric feedback cooling of a laser-trapped nanoparticle," Physical review letters **109**, 103603 (2012).

[31] N. Kiesel, F. Blaser, U. Delić, D. Grass, R. Kaltenbaek, and M. Aspelmeyer, "Cavity cooling of an optically levitated submicron particle," Proceedings of the National Academy of Sciences **110**, 14180–14185 (2013).

[32] D. E. Chang, C. A. Regal, S. B. Papp, D. J. Wilson, J. Ye, O. Painter, H. J. Kimble, and P. Zoller, "Cavity opto-mechanics using an optically levitated nanosphere," Proceedings of the National Academy of Sciences **107**, 1005–1010 (2010), https://www.pnas.org/content/107/3/1005.full.pdf.

[33] S. Chakram, Y. S. Patil, L. Chang, and M. Vengalattore, "Dissipation in ultrahigh quality factor sin membrane resonators," 10.1103/PhysRevLett.112.127201, 1311.1234v1.

[34] L. Neuhaus, A. G. Kuhn, S. Zerkani, J. Teissier, D. García-Sánchez, S. Deléglise,

T. Briant, P. . Cohadon, and A. Heidmann, "Fabry-perot cavity optomechanics with ultrahigh mechanical-q-factor quartz micropillars at cryogenic temperature," in *2013 Conference on Lasers Electro-Optics Europe International Quantum Electronics Conference CLEO EUROPE/IQEC* (2013) pp. 1–1.

[35] J. Liu, K. Usami, A. Naesby, T. Bagci, E. S. Polzik, P. Lodahl, and S. Stobbe, "High-q optomechanical gaas nanomembranes," Applied Physics Letters **99**, 243102 (2011), https://doi.org/10.1063/1.3668092.

[36] G. Ranjit, M. Cunningham, K. Casey, and A. A. Geraci, "Zeptonewton force sensing with nanospheres in an optical lattice," Phys. Rev. A **93**, 053801 (2016).

[37] F. Monteiro, S. Ghosh, A. G. Fine, and D. C. Moore, "Optical levitation of 10-ng spheres with nano- g acceleration sensitivity," Physical Review A **96** (2017), 10.1103/physreva.96.063841.

[38] P. Asenbaum, S. Kuhn, S. Nimmrichter, U.Sezer, and M. Arndt, "Cavity cooling of free silicon nanoparticles in high vacuum," Nature communications **4**, 1–7 (2013).

[39] U. Delić, M. Grass, D.and Reisenbauer, T. Damm, M. Weitz, N. Kiesel, and M. Aspelmeyer, "Levitated cavity optomechanics in high vacuum," Quantum Science and Technology **5**, 025006 (2020).

[40] D. Burnham and D. McGloin, "Holographic optical trapping of aerosol droplets," Optics express **14**, 4175–4181 (2006).

[41] M.Beck, "Overcoming stiction forces: Launching silica microspheres into anoptical trap," B.S. thesis (2012).

[42] H. Park and T. W. LeBrun, "Optical trap loading of dielectric microparticles in air." Journal of visualized experiments : JoVE (2017), 10.3791/54862.

[43] D. P. Atherton, *Sensitive Force Measurements With Optically Trapped Micro-Spheres in High Vacuum*, Ph.D. thesis, University of Nevada, Reno (2015).

[44] L.-O. Heim, J. Blum, M. Preuss, and H.-J. Butt, "Adhesion and friction forces between spherical micrometer-sized particles," Phys. Rev. Lett. **83**, 3328–3331 (1999).

[45] U. Sezer, L. Wörner, J. Horak, L. Felix, J. Tüxen, C. Götz, A. Vaziri, M. Mayor, and M. Arndt, "Laser-induced acoustic desorption of natural and functionalized

biochromophores," Analytical chemistry **87**, 5614–5619 (2015).

[46] D. S. Bykov, P. Mestres, L. Dania, L. Schmöger, and T. E. Northup, "Direct loading of nanoparticles under high vacuum into a paul trap for levitodynamical experiments," Applied Physics Letters **115**, 034101 (2019).

[47] P. Mestres, J. Berthelot, M. Spasenović, J. Gieseler, L. Novotny, and R. Quidant, "Cooling and manipulation of a levitated nanoparticle with an optical fiber trap," Applied Physics Letters **107**, 151102 (2015).

[48] M. J. Renn, D. Montgomery, O. Vdovin, D. Z. Anderson, C. E. Wieman, and E. A. Cornell, "Laser-guided atoms in hollow-core optical fibers," Phys. Rev. Lett. **75**, 3253–3256 (1995).

[49] F. Benabid, J. Knight, and P. S. J. Russell, "Particle levitation and guidance in hollow-core photonic crystal fiber," Optics express **10**, 1195–1203 (2002).

[50] D. Grass, *Levitated optomechanics in vacuum using hollow core photonic crystal fibers and optical cavities*, Ph.D. thesis, University of Vienna (2018).

[51] P. S. J. Russell, "Photonic-crystal fibers," Journal of lightwave technology **24**, 4729–4749 (2006).

[52] A. Ermolov, K. Mak, F. Tani, P. Hölzer, J. Travers, and P. S. J. Russell, "Low loss hollow optical-waveguide connection from atmospheric pressure to ultra-high vacuum," Applied Physics Letters **103**, 261115 (2013).

[53] S. W. M.Eng., *Bericht zum Design und Tolerancing einer Fokussierlinse*, Tech. Rep. (Asphericon, 2017).

[54] F. Ricci, *Levitodynamics toward force nano-sensors in vacuum*, Ph.D. thesis, Universitat Politècnica de Catalunya (2019).

[55] U. Delić, *Cavity cooling by coherent scattering of a levitated nanosphere in vacuum"*, Ph.D. thesis, University of Vienna (2019).

[56] NKT Photonics, *HC-1060-FUD*, Tech. Rep. (NKT Photonics, 2019).

[57] L. Magrini and et al, (2020), in preparation.

[58] P. Chiggiato, "Materials and properties iv outgassing," CERN Accelerator School (CAS) on Vacuum for Particle Accelerators (2017).

[59] J. Young, "Outgassing characteristics of stainless steel and aluminum with different surface treatments," Journal of Vacuum Science and Technology **6**, 398–

400 (1969).

Vacuum system design

This appendix will give insights to parameters that need to be taken into account when designing a vacuum system for ultra high vacuum and below. The main consideration is the desired final vacuum level, which decides most other parameters.

Pressure Limits

The base pressure of a vacuum system is limited by multiple factors. Leaks, contaminants, gas diffusion through walls as well as surface outgassing are the usual factors. The base pressure can be calculated in a simple fashion if these values are known, it is given by the formula:

$$P_{base} = \frac{Q_{out} + Q_{leak} + Q_{diff}}{S_{eff}} \tag{39}$$

where S_{eff} is the effective pumping speed, which is limited by conductance.

In UHV systems the main factor of this equation is the surface outgassing. The amount of outgassing per unit of area varies strongly depending on the material. For this reason the use high outgassing materials, like most polymers, should be avoided in UHV systems. The surface of the vacuum chamber is usually the largest contributing surface, which makes it necessary to use low outgassing materials, such as stainless steel or aluminium, to construct vacuum chambers. A comprehensive study of material outgassing made at CERN [58], where an overview of the outgassing process is given, places the outgassing for baked stainless steel at $q_{out,steel} = 3 * 10^{-12} \frac{mBar*l}{cm^2 s}$, with a value of $q_{out,steel} = 4 * 10^{-14} \frac{mBar*l}{cm^2 s}$ measured in [59] after extended high temperature bakeout. With this value and the internal surface area of a vacuum system the necessary pumping speed for a desired ultimate pressure can be calculated.

$$P_{base} = \frac{Q_{out}}{S_{eff}} \tag{40}$$

Pumping systems

Once the rate of outgassing for a given system is determined the correct pump has to be chosen to reach the desired pressure. For the choice of pumps it is necessary to keep in mind that the pumping speed will be limited by the conductance of the connecting flange or pipe. The effective pumping speed dependent on pumping speed and conductance is given by:

$$S_{eff} = \frac{SC}{S+C} \tag{41}$$

with a conductance in the molecular flow regime of $C = \frac{\pi \bar{v}_{therm} d^3}{12l}$. Due to this relationship the effective pumping speed of a pump cannot exceed the conductance of the orifice it is connected to. For example the pumping speed of a 100l/s pump is reduced to 50l/s when connected to a 100l/s orifice.

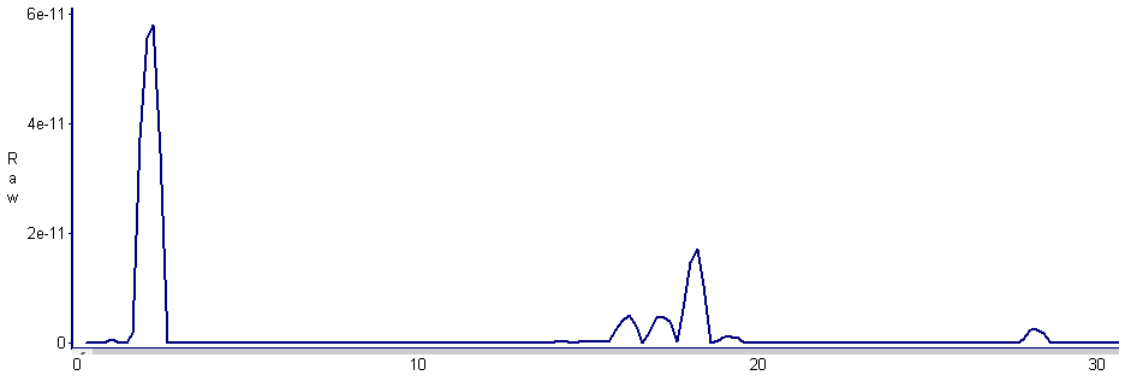

Figure 32: Mass spectrum of residual gas in a UHV chamber. It is visible that the greatest contribution stems from H_2 gas that is a product of outgassing. Residual traces of water and nitrogen are still present in the system, but are over a factor 4 smaller.

In a vacuum system limited by outgassing the majority of residual gas in a UHV system will be the hydrogen released from the chamber walls. A residual gas scan in Fig.32 shows this for a system at 10^{-10} mBar pressure. To reach such low and even lower pressures the correct pumping system is necessary. Most vacuum systems rely on turbomolecular pumps to reach the low ranges of high vacuum or ultrahigh vacuum. However these pumps usually exhibit bad

compression for H_2. For this reason either another pump with better pumping speed for that particular gas, or a way to prevent outgassing is required.

- **Sublimation Getter Pumps**

  Sublimation getter pumps function by evaporating a getter material, most commonly titanium, that deposits on the walls of the vacuum system. There the surface created binds the residual gas of the vacuum system, as molecules stick to the surfaces. While this type of pump achieves excellent pumping speeds due to the large coverage it can supply it relies on coating the interior of the system with a metal film. This makes sublimation pumps unsuitable for with sensitive optical equipment.

- **Non evaporative Getter Pumps**

  Getter pumps bind gas using chemical reactions. With proper choice of material the reactivity for the typical residual gases can be maximized, resulting in high pumping speeds. These pumps are usually used over titanium sublimation pumps if evaporation of metals and surface depositing of metal films are undesirable.

- **Ion getter Pumps**

  Such pumps utilize gas discharge to ionize gas particles. These are caught in an electrical potential and implants them in a getter cathode. In this fashion effective pumping of noble gases is achieved in ion pumps. These pumps are often used in conjunction with titanium sublimation pumps or non evaporative getter pumps, as they provide the ability to pump non-getterable gases. Due to the nature of ionization shielding can become necessary to prevent experimental samples from becoming charged.

For an optical levitation experiment requiring ultrahigh vacuum a combination of non evaporative and shielded ion getter pump promises to supply the required pumping speed for H_2 and noble gases, while a turbomolecular pump can efficiently remove nitrogen and hydrocarbons.

Example Calculation

The predicted base pressure of an octagon chamber with a surface area of approximately 3000cm^2 made out of stainless steel with a hydrogen outgassing rate of $q_{out,steel} = 1 * 10^{-13} \frac{mBar*l}{cm^2 s}$, a value achievable at bakeout temperatures of 250°C, requires a minimal pumping rate to achieve 10^{-11}mBar of:

$$S_{eff,min} = \frac{q_{out,steel} * A}{P} \approx 300 L/s. \tag{42}$$

A pump with higher pumping speed might be chosen to ensure that deviations from the surface area do not affect performance. Alternatively the whole vacuum system can be vacuum fired at high temperatures, which has been shown to reduce outgassing rates below $10^{-15} \frac{mBar*l}{cm^2 s}$ [59] [58].

For vacuum systems consisting of different materials, for example glass viewports or copper wire, the surface areas have to be matched with the material specific outgassing rates to calculate the required pumping speed. Information on the primarily outgassed substance should also be taken into consideration, to allow the correct pump choice to be made. In general combination pumps are becoming more widely used, which cover a large range of gases and provide good pumping speeds. Reaching low UHV and even XHV pressures without incurring extreme experimental limitations has never been easier.

Asphere

$$z(h)=\frac{h^2}{R\left(1+\sqrt{1-(1+k)\frac{h^2}{R^2}}\right)}+\sum_{i=2}^{n} A_{2i}\,h^{2i}$$

R	=	5.430 ±0.005
k	=	-1
A_4	=	0.000334
A_6	=	1.27e-007
A_8	=	-5.47e-008
A_{10}	=	-9.96e-010
A_{12}	=	1.895e-011

h	z(h)
0.0	-0.000000
1.0	-0.092415
2.0	-0.373661
3.0	-0.855468
4.0	-1.555009
5.0	-2.486293
6.0	-3.642857
6.35	-4.094994

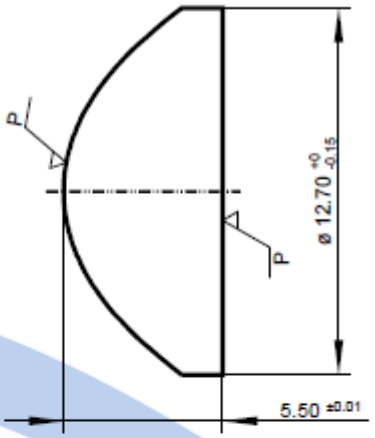

1) all dimensions in mm

i) comments:
- diameter tolerance +0/-0,15 added
- cleanliness 5/ 5 x 0,25; L3 x 0,04, E0,3 added on both sides
- protective chamfer 0,2–0,5 added on 2nd

1st	Material Specification	2nd
Asphere R = 5.43 ±0.005 cx øe 11.2 no chamfer 3/ - (1) RMSi < 50 nm full surface non-contact measurement 4/ 5.5' 5/ 5 x 0.25; L3 x 0.04; E0.3 Ⓛ ARDS @1064 nm R_{max}<0,5% AOI=0°	S-LAH58 n_d = 1,882997 v_d = 40,77 0/ - 1/ - 2/ -	R = infinite øe 10 protective chamfer 0.2–0.5 3/ 2 (1) RMSi < 50 nm 4/ - 5/ 5 x 0.25; L3 x 0.04; E0.3 Ⓛ ARDS @1064 nm R_{max}<0,5% AOI=0°

170435-000-03A (26.09.2017)			asphericon
Scale 5 : 1	Ind. acc. ISO 10110	26.09.2017 CKA	